ORIGINAL PAPER

Predicting Wax Deposition in Oil Pipelines: A Computational Model Incorporating Heat and Mass Transfer Effects

Francis Oketch Ochieng[1] · Mathew Ngugi Kinyanjui[1] · Phineas Roy Kiogora[1] · Jeconia Okelo Abonyo[1]

Abstract

A novel computational model is presented for predicting wax deposition in crude oil pipelines, accounting for the complex interplay of multiphase flow scenarios involving water-in-oil emulsions, wax precipitation kinetics, molecular diffusion, and shear dispersion. The governing equations are solved numerically by the bivariate spectral collocation method using Chebyshev-Gauss-Lobatto grid points. The model's predictive capabilities are evaluated by investigating the impact of various flow parameters, including Reynolds number (Re), Grashof number (Gr), Schmidt number (Sc), and Weber number (We), on the flow variables, wall shear stress, and heat and mass fluxes. The key findings reveal that wax deposition is significantly influenced by the intricate interplay of flow conditions, wax precipitation kinetics, and heat and mass transfer phenomena. Notably, increasing Reynolds number from 2 to 6.5 leads to at most 5% increase in wax deposition, while increasing mass Grashof number from 4 to 16 results in at most 10% reduction in wax accumulation. Similarly, higher Schmidt numbers (Sc > 1) and Weber numbers (We > 1) tend to mitigate wax deposition by at most 15% and 6%, respectively. These insights offer valuable guidance for optimizing pipeline operations, designing effective wax control strategies, and enhancing pipeline integrity management in field-scale crude oil transportation systems.

List of Symbols
Roman Symbols

Cp	Specific heat at constant pressure, [J/(kg K)]
D_p	Shear dispersion coefficient, [m]
D_d	Molecular diffusion coefficient of wax, [m^2/s]
$\bar{d}$	Dimensionless diameter of water droplet

✉ Francis Oketch Ochieng
   francokech@gmail.com

1   Department of Pure and Applied Mathematics, Jomo Kenyatta University of Agriculture and Technology, Nairobi, Kenya

🖄 Springer

$\mathbf{g}$	Gravitational acceleration, [m/s^2]
k	Thermal conductivity, [W/m K]
K_1	Smooth and positive function of fluid temperature, [1/s]
K_2	Smooth and positive function of fluid temperature, [1/Pa]
P	Dimensionless pressure
Q	Volume flow rate, [m^3/s]
R	Radius of clean pipe, [m]
$(\bar{r}, \bar{z})$	Dimensionless cylindrical co-ordinate variables
$\bar{t}$	Dimensionless time
(u, v)	Dimensionless velocity components
Da	Darcy number
Ec	Eckert number
Gr$_T$	Thermal Grashof number
Gr$_C$	Mass Grashof number
Pr	Prandtl number
Pe	Peclet number
Re	Reynolds number
St	Stanton number
Sc	Schmidt number
We	Weber number

Greek Symbols

α_{avg}	Average aspect ratio of the wax crystals
α	Angle of elevation of pipeline from the horizontal
β_T	Thermal volume expansion coefficient, [1/K]
β_C	Concentration volume expansion coefficient, [m^3/kg]
μ	Coefficient of dynamic viscosity, [Nsm^{-2}]
ϕ	Dimensionless concentration of non-aggregated wax
ϕ_{i}	Proportion of volume occupied by the i-th phase.
ρ	Fluid density, [Kg/m^3]
σ	Surface tension coefficient, [N/m]
Θ	Dimensionless temperature

Subscripts

f	Fluid phase
water	Water droplets
oil	Crude oil
gel	Deposit or gel-like layer
mix	Mixture fluid
wall	Condition at the solid–liquid interface
∞	Condition at the free-stream

Introduction

Wax deposition is a significant challenge in the transportation of waxy crude oils through pipelines [1, 2]. As the crude oil cools, wax crystals precipitate and adhere to the pipe wall, forming a gel-like deposit that can reduce flow rate, increase pressure drop, and eventually lead to potential pipeline blockage and even pipeline rapture [1, 3]. This can cause signif-

icant operational and economic losses, disruptions to the energy supply chain, as well as environmental damage due to potential spills [4–7].

Wax deposition is a complex process that is influenced by a number of factors, including the composition of the crude oil, the flow conditions, and the temperature profile of the pipeline [8, 9]. Accurately predicting wax deposition is essential for designing and operating pipelines that are safe and reliable [2].

Several models have been developed for predicting wax deposition in oil pipelines. In particular, Kim et al. [10] modeled the consolidation of wax deposition for progressive cavity pump using computational fluid dynamics. Mrinal et al. [11] investigated a transient three-dimensional computational fluid dynamics model of a progressive cavity pump. Waheed and Megahed [12] studied the heat transfer mechanism to the non-Newtonian micropolar slip fluid flow over a stretching sheet in the presence of the melting heat transfer with heat generation or absorption in the slip flow regime. Singh et al. [13] studied the formation and aging of the wax deposit by performing a series of laboratory flow loop experiments and considering externally cooled pipeline walls.

Stubsjoen [14] studied both the numerical and analytical modeling of paraffin wax in crude oil pipelines. Fusi [15] studied the unsteady flow of waxy crude oil in a laboratory test loop. Banki et al. [16] investigated the numerical modeling of wax deposition in oil pipelines for the laminar flow regime based on the enthalpy-porosity approach. Zhang et al. [17] developed a wax deposition model to predict the temperature field and location of wax deposition based on a heat-fluid coupling process for a typical rod-tubing-casing-cement-formation with the borehole axis as the center. Ying et al. [18] studied heat transfer analysis of oil phase-change during overhead pipeline shutdown. Magnini and Matar [19] investigated the deposition of wax in crude oil pipelines through interface-resolved numerical simulations.

In their work on numerical investigations of wax deposition under laminar flow conditions, Boucetta et al. [20] introduced a novel numerical approach for predicting the temporal and spatial evolution of wax deposits. Their method is firmly grounded in theoretical principles, incorporating energy and momentum balance equations along with Fick's law-based molecular diffusion modeling. The study's findings indicate that extending deposition time and porosity significantly increases wax deposit content and pressure drop while reducing fluid temperature, heat transfer coefficient, and flow rate. Additionally, it was demonstrated that wax deposits tend to concentrate over a short axial length.

Previous studies have primarily focused on wax deposition in single-phase waxy crude oil pipelines. However, the issue also arises in multiphase flows, including water-oil or gas-oil
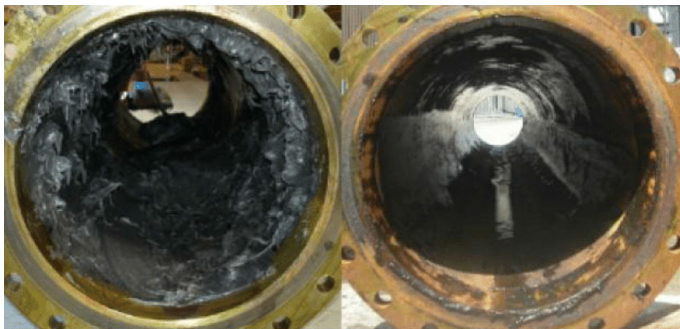

Fig. 1 A pipeline cross-section depicting wax deposition in oil pipelines

two-phase flows and water-gas-oil three-phase flows, which are prevalent in the oil and gas industry. Oil–water two-phase flows have garnered significant attention due to the increasing water content of oil-bearing rocks during crude oil extraction. Existing wax deposition models are incompatible with real-world oil pipelines due to numerous research gaps. Therefore, further research on the computational modeling of wax deposition in oil pipelines with heat and mass transfer is crucial. Conventional wax deposition models often employ simplified assumptions and fail to capture the complex interplay of multiphase flow of oil, water, and wax, the kinetics of wax precipitation, molecular diffusion, shear dispersion, and heat and mass transfer phenomena that govern wax precipitation and deposition.

To address these limitations, we present a novel computational model for predicting wax deposition in oil pipelines. This model incorporates complex phenomena, providing a more comprehensive and accurate prediction of wax deposition behavior under a wide range of operating conditions. Based on the bivariate spectral collocation method, the model can simulate wax deposition in pipelines transporting waxy crude oil. This study stands out for its incorporation of several novel aspects, including: (i) a detailed description of multiphase flow of oil, water, and wax, including water-in-oil emulsions, (ii) a consideration of wax precipitation kinetics, and (iii) the inclusion of molecular diffusion and shear dispersion as the mechanisms responsible for wax deposition.

The remaining sections of the paper are structured in the following manner: Sect. 3 presents the formulation of the mathematical model for the flow of waxy crude oil in pipeline systems, Sect. 4 presents the numerical techniques used to solve the model equations, Sect. 5 presents the study results and a comprehensive discussion of the results. The results are validated in Sect. 6. Finally, the summary and conclusions drawn from this study are outlined in Sect. 7.

Mathematical Formulation

In this study, we examine the two-dimensional unsteady flow of waxy crude oil in a model of a pipeline with a semi-infinite length, circular cross-section, and an inner radius denoted as R, as depicted in Fig. 2. The pipeline is inclined at an angle denoted as α with respect to the horizontal. We employ a cylindrical coordinate system denoted as (r, θ, z), where r represents the radial distance measured from the center of the pipeline, θ represents the tangential direction, and z indicates the axial direction. Initially, at time $t \leq 0$, we introduce waxy crude oil at a uniform temperature T_∞ at the pipeline inlet. The inner pipeline surface, assumed to be smooth, impermeable, and rigid, is maintained at a uniform temperature T_{wall}. The temperature T_{wall} can either be higher or lower than T_∞.

The boundary between the discrete solid phase and the continuous fluid phase is a sharp interface. The outwardly drawn unit normal vector to this interface is given by $\hat{\mathbf{n}} = \vec{\nabla}\phi_{\text{oil}} / \left| \vec{\nabla}\phi_{\text{oil}} \right|$. The fluid phase consists of three pseudo-components: oil, wax, and emulsions.

We employ the Pseudo-Single Phase (PSP) approach, which treats the water-oil-gel three-phase fluid mixture as a single-phase fluid. This assumption is valid when the phases are well-mixed and there is minimal interaction between them. The physical properties of the fluid mixture, such as viscosity and thermal conductivity, are determined by averaging the corresponding properties of water, oil, and gel, weighted by their respective volume fractions, as presented in the studies by Yang [21], Zheng et al. [22], and Ochieng et al. [23]. This averaging technique, known as the principle of volume averaging, is commonly used to estimate the effective properties of heterogeneous mixtures. For thermal conductivity, the
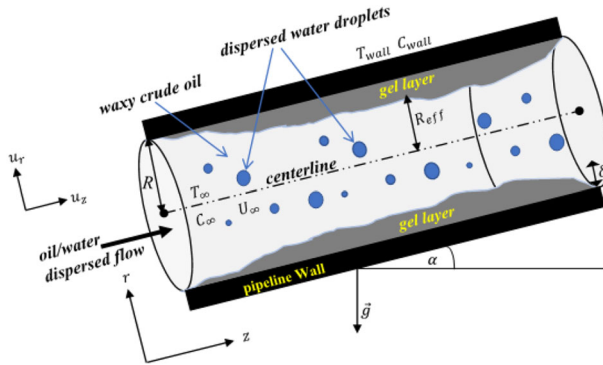
Fig. 2 Schematic diagram for the flow of waxy crude oil in the pipeline

averaging is based on the Maxwell-Garnett model [24], which assumes that the phases are embedded within a continuous matrix. The thermal conductivity of the mixture depends on the thermal conductivities of the phases, the volume fraction of the dispersed phase, and the shape of the dispersed phase particles. Applying these averaging techniques yields the following equations:

$$\rho_{\mathrm{f}} = (1 - \phi_{\mathrm{water}}) \rho_{\mathrm{oil}} + \phi_{\mathrm{water}} \rho_{\mathrm{water}} \tag{1}$$

$$\rho_{\mathrm{mix}} = \left(1 - \phi_{\mathrm{gel}}\right) \rho_{\mathrm{f}} + \phi_{\mathrm{gel}} \rho_{\mathrm{gel}} \tag{2}$$

$$\mu_{\mathrm{f}} = (1 - \phi_{\mathrm{water}}) \mu_{\mathrm{oil}} + \phi_{\mathrm{water}} \mu_{\mathrm{water}} \tag{3}$$

$$\mu_{\mathrm{mix}} = \left(1 - \phi_{\mathrm{gel}}\right) \mu_{\mathrm{f}} + \phi_{\mathrm{gel}} \mu_{\mathrm{gel}} \tag{4}$$

$$(\beta_{\mathrm{T}})_{\mathrm{f}} = (1 - \phi_{\mathrm{water}}) (\beta_{\mathrm{T}})_{\mathrm{oil}} + \phi_{\mathrm{water}} (\beta_{\mathrm{T}})_{\mathrm{water}} \tag{5}$$

$$(\beta_{\mathrm{T}})_{\mathrm{mix}} = \left(1 - \phi_{\mathrm{gel}}\right) (\beta_{\mathrm{T}})_{\mathrm{f}} + \phi_{\mathrm{gel}} (\beta_{\mathrm{T}})_{\mathrm{gel}} \tag{6}$$

$$(\beta_{\mathrm{C}})_{\mathrm{f}} = (1 - \phi_{\mathrm{water}}) (\beta_{\mathrm{C}})_{\mathrm{oil}} + \phi_{\mathrm{water}} (\beta_{\mathrm{C}})_{\mathrm{water}} \tag{7}$$

$$(\beta_{\mathrm{C}})_{\mathrm{mix}} = \left(1 - \phi_{\mathrm{gel}}\right) (\beta_{\mathrm{C}})_{\mathrm{f}} + \phi_{\mathrm{gel}} (\beta_{\mathrm{C}})_{\mathrm{gel}} \tag{8}$$

$$(Cp)_{\mathrm{f}} = \frac{(1 - \phi_{\mathrm{water}}) \rho_{\mathrm{oil}} (Cp)_{\mathrm{oil}} + \phi_{\mathrm{water}} \rho_{\mathrm{water}} (Cp)_{\mathrm{water}}}{\rho_{\mathrm{f}}} \tag{9}$$

$$(Cp)_{\mathrm{mix}} = \frac{\left(1 - \phi_{\mathrm{gel}}\right) \rho_{\mathrm{f}} (Cp)_{\mathrm{f}} + \phi_{\mathrm{gel}} \rho_{\mathrm{gel}} (Cp)_{\mathrm{gel}}}{\rho_{\mathrm{mix}}} \tag{10}$$

$$k_{\mathrm{f}} = \left[\frac{k_{\mathrm{water}} + 2k_{\mathrm{oil}} + 2\phi_{\mathrm{water}} (k_{\mathrm{water}} - k_{\mathrm{oil}})}{k_{\mathrm{water}} + 2k_{\mathrm{oil}} - \phi_{\mathrm{water}} (k_{\mathrm{water}} - k_{\mathrm{oil}})} \right] k_{\mathrm{oil}} \tag{11}$$

$$k_{\mathrm{mix}} = \left[\frac{k_{\mathrm{gel}} + 2k_{\mathrm{f}} + 2\phi_{\mathrm{gel}} \left(k_{\mathrm{gel}} - k_{\mathrm{f}}\right)}{k_{\mathrm{gel}} + 2k_{\mathrm{f}} - \phi_{\mathrm{gel}} \left(k_{\mathrm{gel}} - k_{\mathrm{f}}\right)} \right] k_{\mathrm{f}}, \tag{12}$$

where the subscript mix denotes "mixture fluid" and f denotes "fluid phase".

The following assumptions are made in this study: no gas is present in the pipeline, the flow is axisymmetric, molecular diffusion and shear dispersion are the only wax deposition mechanisms, the fluid particles do not slip at the boundary of the fluid-solid phase, the thermophysical properties are constants except the variation of density with temperature and concentration in the body force term. Hence, Boussinesq's approximation is utilized in modeling the flow in the boundary layer.

Using the assumptions above, we obtain the following dimensionless equations [23]:

Equation of continuity

$$\frac{\partial (\bar{r}u)}{\partial \bar{r}} + \frac{\partial (\bar{r}v)}{\partial \bar{z}} = 0.$$ (13)

Equations of conservation of linear momentum

$$\frac{\partial u}{\partial \bar{t}} + u\frac{\partial u}{\partial \bar{r}} + v\frac{\partial u}{\partial \bar{z}} = -\frac{\partial P}{\partial \bar{r}} - \frac{\chi_2}{(\text{Re} \cdot \text{Da})}u + \frac{\chi_1}{\text{We}}R\bar{K}\frac{\partial \phi_{\text{oil}}}{\partial \bar{r}}$$

$$+\frac{\chi_2}{\text{Re}}\left(2\frac{\partial^2 u}{\partial \bar{r}^2} + \frac{\partial^2 u}{\partial \bar{z}^2} + \frac{\partial^2 v}{\partial \bar{r}\partial \bar{z}} + \frac{2}{\bar{r}}\frac{\partial u}{\partial \bar{r}} - \frac{2}{\bar{r}^2}u\right)$$

$$+\chi_3\frac{\text{Gr}_\text{T}}{\text{Re}^2}\cos(\alpha)\Theta + \chi_4\frac{\text{Gr}_\text{C}}{\text{Re}^2}\cos(\alpha)\phi$$ (14)

$$\frac{\partial v}{\partial \bar{t}} + u\frac{\partial v}{\partial \bar{r}} + v\frac{\partial v}{\partial \bar{z}} = -\frac{\partial P}{\partial \bar{z}} - \frac{\chi_2}{(\text{Re} \cdot \text{Da})}v + \frac{\chi_1}{\text{We}}R\bar{K}\frac{\partial \phi_{\text{oil}}}{\partial \bar{z}}$$

$$+\frac{\chi_2}{\text{Re}}\left(\frac{\partial^2 v}{\partial \bar{r}^2} + 2\frac{\partial^2 v}{\partial \bar{z}^2} + \frac{\partial^2 u}{\partial \bar{r}\partial \bar{z}} + \frac{1}{\bar{r}}\frac{\partial u}{\partial \bar{z}} + \frac{1}{\bar{r}}\frac{\partial v}{\partial \bar{r}}\right)$$

$$+\chi_3\frac{\text{Gr}_\text{T}}{\text{Re}^2}\sin(\alpha)\Theta + \chi_4\frac{\text{Gr}_\text{C}}{\text{Re}^2}\sin(\alpha)\phi$$ (15)

Equation of energy

$$\frac{\partial \Theta}{\partial \bar{t}} + u\frac{\partial \Theta}{\partial \bar{r}} + v\frac{\partial \Theta}{\partial \bar{z}} = \frac{\chi_5}{\text{Pe}}\left(\frac{\partial^2 \Theta}{\partial \bar{r}^2} + \frac{1}{\bar{r}}\frac{\partial \Theta}{\partial \bar{r}} + \frac{\partial^2 \Theta}{\partial \bar{z}^2}\right)$$

$$-\text{St}\frac{\chi_6}{\bar{d}}\Theta + \chi_7\frac{\text{Ec}}{\text{Re}}\left[2\left(\frac{\partial u}{\partial \bar{r}}\right)^2 + 2\left(\frac{u}{\bar{r}}\right)^2\right.$$

$$\left.+2\left(\frac{\partial v}{\partial \bar{z}}\right)^2 + \left(\frac{\partial v}{\partial \bar{r}} + \frac{\partial u}{\partial \bar{z}}\right)^2\right]$$ (16)

Equation of wax concentration

$$\frac{\partial \phi}{\partial \bar{t}} + u\frac{\partial \phi}{\partial \bar{r}} + v\frac{\partial \phi}{\partial \bar{z}}$$

$$= \varepsilon_\text{p}\left[(1-\alpha_\text{m})(\phi - \bar{C}_\text{d})\left(\frac{\partial^2 v}{\partial \bar{r}^2} + \frac{1}{\bar{r}}\frac{\partial v}{\partial \bar{r}}\right)\right.$$

$$+\left\{(1-\alpha_\text{m})\left(\frac{\partial \phi}{\partial \bar{r}} - \frac{d\bar{C}_\text{d}}{d\Theta}\frac{\partial \Theta}{\partial \bar{r}}\right) - (\phi - \bar{C}_\text{d})\frac{\partial \alpha_\text{m}}{\partial \bar{r}}\right\}$$

$$\left.*\frac{\partial v}{\partial \bar{r}}\right] + \frac{1}{\text{Re} \cdot \text{Sc}}\left[\frac{d\bar{C}_\text{d}}{d\Theta}\left(\frac{\partial^2 \Theta}{\partial \bar{r}^2} + \frac{1}{\bar{r}}\frac{\partial \Theta}{\partial \bar{r}} + \frac{\partial^2 \Theta}{\partial \bar{z}^2}\right)\right.$$

$$\left.+\frac{d^2\bar{C}_\text{d}}{d\Theta^2}\left\{\left(\frac{\partial \Theta}{\partial \bar{r}}\right)^2 + \left(\frac{\partial \Theta}{\partial \bar{z}}\right)^2\right\}\right]$$ (17)

Equation of wax precipitation kinetics

$$\frac{\partial \alpha_\text{m}}{\partial \bar{t}} + u\frac{\partial \alpha_\text{m}}{\partial \bar{r}} + v\frac{\partial \alpha_\text{m}}{\partial \bar{z}} = [1 - \alpha_\text{m}]\bar{K}_1(\Theta)$$

$$-\alpha_\text{m}\frac{\text{Re}}{\chi_2}\left(\frac{\partial v}{\partial \bar{r}}\right)^2 \bar{K}_2(\Theta)$$ (18)

Equation of oil volume fraction

$$\frac{\partial \phi_{\text{oil}}}{\partial \bar{t}} + u \frac{\partial \phi_{\text{oil}}}{\partial \bar{r}} + v \frac{\partial \phi_{\text{oil}}}{\partial \bar{z}} = 0 \tag{19}$$

Equation of deposit growth

$$\frac{d\bar{\delta}}{d\bar{t}} = \phi_1 \frac{(1 - f(x))}{x} \left(\frac{1}{\text{Re} \cdot \text{Sc}} \frac{d\bar{C}_d}{d\Theta} \frac{\partial \Theta}{\partial \bar{r}} \bigg|_{\bar{r}=\bar{R}_{\text{eff}}} \right) \tag{20}$$

Equation of deposit aging

$$\frac{dx}{d\bar{t}} = \phi_1 f(x) \frac{2(1-\bar{\delta})}{\bar{\delta}(2-\bar{\delta})} \left[\frac{1}{\text{Re} \cdot \text{Sc}} \frac{d\bar{C}_d}{d\Theta} \frac{\partial \Theta}{\partial \bar{r}} \right.$$

$$\left. + \varepsilon_p (1 - \alpha_m) (\phi - \bar{C}_d) \frac{\partial v}{\partial \bar{r}} \right]_{\bar{r}=\bar{R}_{\text{eff}}}. \tag{21}$$

The following dimensionless numbers and parameters are utilized in the model equations (13)−(21):

$$\chi_1 = \frac{\rho_f}{\rho_{\text{mix}}}, \quad \chi_2 = \frac{\mu_{\text{mix}}}{\mu_f} \frac{\rho_f}{\rho_{\text{mix}}}, \quad \chi_3 = \frac{(\beta_T)_{\text{mix}}}{(\beta_T)_f}, \tag{22}$$

$$\chi_4 = \frac{(\beta_C)_{\text{mix}}}{(\beta_C)_f}, \quad \chi_5 = \frac{\alpha_{\text{mix}}}{\alpha_f} = \frac{k_{\text{mix}}}{k_f} \frac{\rho_f}{\rho_{\text{mix}}} \frac{(Cp)_f}{(Cp)_{\text{mix}}}, \tag{23}$$

$$\chi_6 = \frac{\rho_f}{\rho_{\text{mix}}} \frac{(Cp)_f}{(Cp)_{\text{mix}}}, \quad \chi_7 = \frac{\mu_{\text{mix}}}{\mu_f} \chi_6, \quad \varepsilon_p = \frac{D_p}{R}, \tag{24}$$

$$\phi_0 = \frac{(C_\infty - \rho_{\text{gel}})}{(C_{\text{wall}} - C_\infty)}, \quad \phi_1 = \frac{(C_{\text{wall}} - C_\infty)}{\rho_{\text{gel}}}, \tag{25}$$

$$\alpha_{\text{avg}} = 1.684 - 0.323 \ln Q, \tag{26}$$

$$\text{Re} = \frac{\rho_f U_\infty R}{\mu_f}, \quad \text{Gr}_T = \frac{\rho_f^2 g (\beta_T)_f (\Delta T) R^3}{\mu_f^2}, \tag{27}$$

$$\text{Gr}_C = \frac{\rho_f^2 g (\beta_C)_f (\Delta C) R^3}{\mu_f^2}, \quad \text{Ec} = \frac{U_\infty^2}{(Cp)_f \Delta T}, \tag{28}$$

$$\text{Pr} = \frac{\mu_f}{\rho_f \alpha_f}, \quad \text{Pe} = \frac{U_\infty R}{\alpha_f}, \quad \text{St} = \frac{h_r}{\rho_f U_\infty (Cp)_f}, \tag{29}$$

$$\text{Sc} = \frac{\mu_f}{\rho_f D_d}, \quad \text{We} = \frac{\rho_f U_\infty^2 R}{\sigma}, \quad \text{Da} = \frac{\kappa}{R^2}, \tag{30}$$

$$f(x) = \frac{1 - x}{\alpha_{\text{avg}}^2 x^2 - x + 1}. \tag{31}$$

The following thermodynamic model, presented in Cragoe [25] and Al-Ahmad et al. [26], is adopted in this study:

$$\bar{C}_d = \frac{1}{S_f} \left(\frac{0.981 + 0.0677\Theta}{1 - 0.0208\Theta} \right), \tag{32}$$

where $S_f = (0.0077 \text{MW}_{\text{oil}} - 1.737)$ denotes the shift factor while $\text{MW}_{\text{oil}} = \dfrac{6084}{{}^o\text{API} - 5.9}$ denotes the molecular weight of waxy crude oil. In this study, the heavy waxy crude oil with API gravity of $18\,{}^o$API is considered.

The corresponding initial and boundary conditions for the flow are formulated as follows:

$$
\begin{cases}
\dfrac{\partial u}{\partial \bar{r}} = 0, \ \dfrac{\partial v}{\partial \bar{r}} = 0, \ \dfrac{\partial \Theta}{\partial \bar{r}} = 0, & \\[2mm]
\dfrac{\partial \phi}{\partial \bar{r}} = 0, \ \dfrac{\partial \alpha_{\mathrm{m}}}{\partial \bar{r}} = 0, \ \dfrac{\partial \phi_{\mathrm{oil}}}{\partial \bar{r}} = 0 & \text{at } \bar{r} = 0 \\[4mm]
u = 0, \ v = 0, \ \Theta = 1, \ \phi = 1 & \text{at } \bar{r} = 1 \\[4mm]
u = 0, \ v = 1, \ \Theta = 0, \ \phi = 0 & \\[1mm]
\alpha_{\mathrm{m}} = 0, \ \phi_{\mathrm{oil}} = 1 - \phi_{\mathrm{water}} & \text{at } \bar{z} = 0 \\[4mm]
\dfrac{\partial u}{\partial \bar{z}} = 0, \ \dfrac{\partial v}{\partial \bar{z}} = 0, \ \dfrac{\partial \Theta}{\partial \bar{z}} = 0, & \\[2mm]
\dfrac{\partial \phi}{\partial \bar{z}} = 0, \ \dfrac{\partial \alpha_{\mathrm{m}}}{\partial \bar{z}} = 0, \ \dfrac{\partial \phi_{\mathrm{oil}}}{\partial \bar{z}} = 0 & \text{at } \bar{z} = L \\[4mm]
u = 0, \ v = 0, \ \Theta = 0, \ \phi = 0, \ \alpha_{\mathrm{m}} = 0 & \\[1mm]
\bar{\delta} = 0, \ x = 0, \ \phi_{\mathrm{oil}} = 1 - \phi_{\mathrm{water}} & \text{at } \bar{t} = 0.
\end{cases}
\tag{33}
$$

In this study, the physical parameters of engineering interest are the skin friction coefficient (C_f), the local Nusselt number (Nu_z), and the local Sherwood number (Sh_z). These parameters are given in the dimensionless form:

$$
C_f \mathrm{Re} = 2\left(\frac{\partial v}{\partial \bar{r}}\right)_{\bar{r}=1}, \quad \mathrm{Nu}_z = -\left(\frac{\partial \Theta}{\partial \bar{r}}\right)_{\bar{r}=1},
\tag{34}
$$

$$
\mathrm{Sh}_z = -\left(\frac{\partial \phi}{\partial \bar{r}}\right)_{\bar{r}=1}.
\tag{35}
$$

The skin friction coefficient, the local Nusselt number, and the local Sherwood number describe the shear stress, the heat flux rate, and the mass flux rate at the wall of the crude oil pipeline, respectively.

Numerical Solution

The governing equations given by (13)−(21) subject to the boundary and initial conditions (33) are solved numerically using the spectral collocation method. The model equations are discretized in two different ways: temporal discretization and spatial discretization as illustrated below.

Temporal Discretization

The non-linear terms are discretized in time using the Adams-Bashforth second-order method, which is an explicit scheme of second-order accuracy. The linear terms involving spatial derivatives are discretized in time using the Crank-Nicolson method (an implicit numerical scheme of second-order accuracy) while decoupling the governing PDEs to save on computer memory. Finally, the forward Euler method is used to discretize the time derivatives. Hence, the time-discretized numerical schemes are as follows (for $k = 1, 2, 3, \cdots$):

$$\frac{u^{k+1}-u^k}{\Delta\bar{t}} + \frac{1}{2}\left(3u^k\frac{\partial u^k}{\partial\bar{r}} - u^{k-1}\frac{\partial u^{k-1}}{\partial\bar{r}}\right) + \frac{1}{2}\left(3v^k\frac{\partial u^k}{\partial\bar{z}} - v^{k-1}\frac{\partial u^{k-1}}{\partial\bar{z}}\right) + \frac{\partial P^k}{\partial\bar{r}}$$

$$= \frac{\chi_2}{\text{Re}}\left[\frac{1}{2}\left(2\frac{\partial^2 u^{k+1}}{\partial\bar{r}^2} + 2\frac{\partial^2 u^k}{\partial\bar{r}^2}\right) + \frac{1}{2}\left(\frac{\partial^2 u^{k+1}}{\partial\bar{z}^2} + \frac{\partial^2 u^k}{\partial\bar{z}^2}\right) + \frac{\partial^2 v^k}{\partial\bar{r}\partial\bar{z}}\right.$$

$$\left. + \frac{1}{2}\left(\frac{2}{\bar{r}}\frac{\partial u^{k+1}}{\partial\bar{r}} + \frac{2}{\bar{r}}\frac{\partial u^k}{\partial\bar{r}}\right) - \frac{1}{2}\left(\frac{2}{\bar{r}^2}u^{k+1} + \frac{2}{\bar{r}^2}u^k\right)\right]$$

$$- \frac{\chi_2}{(\text{Re}\cdot\text{Da})}\frac{1}{2}\left(u^{k+1}+u^k\right) + \chi_3\frac{\text{Gr}_T}{\text{Re}^2}\cos(\alpha)\Theta^k + \chi_4\frac{\text{Gr}_C}{\text{Re}^2}\cos(\alpha)\phi^k$$

$$+ \frac{\chi_1}{\text{We}}\frac{1}{2}\left[3\left(R\bar{K}\right)^k\frac{\partial(\phi_{\text{oil}})^k}{\partial\bar{r}} - \left(R\bar{K}\right)^{k-1}\frac{\partial(\phi_{\text{oil}})^{k-1}}{\partial\bar{r}}\right] \tag{36}$$

$$\frac{v^{k+1}-v^k}{\Delta\bar{t}} + \frac{1}{2}\left(3u^k\frac{\partial v^k}{\partial\bar{r}} - u^{k-1}\frac{\partial v^{k-1}}{\partial\bar{r}}\right) + \frac{1}{2}\left(3v^k\frac{\partial v^k}{\partial\bar{z}} - v^{k-1}\frac{\partial v^{k-1}}{\partial\bar{z}}\right) + \frac{\partial P^k}{\partial\bar{z}}$$

$$= \frac{\chi_2}{\text{Re}}\left[\frac{1}{2}\left(\frac{\partial^2 v^{k+1}}{\partial\bar{r}^2} + \frac{\partial^2 v^k}{\partial\bar{r}^2}\right) + \frac{1}{2}\left(2\frac{\partial^2 v^{k+1}}{\partial\bar{z}^2} + 2\frac{\partial^2 v^k}{\partial\bar{z}^2}\right) + \frac{\partial^2 u^k}{\partial\bar{r}\partial\bar{z}} + \frac{1}{\bar{r}}\frac{\partial u^k}{\partial\bar{z}}\right.$$

$$\left. + \frac{1}{2}\left(\frac{1}{\bar{r}}\frac{\partial v^{k+1}}{\partial\bar{r}} + \frac{1}{\bar{r}}\frac{\partial v^k}{\partial\bar{r}}\right)\right] - \frac{\chi_2}{(\text{Re}\cdot\text{Da})}\frac{1}{2}\left(v^{k+1}+v^k\right) + \chi_3\frac{\text{Gr}_T}{\text{Re}^2}\sin(\alpha)\Theta^k$$

$$+ \chi_4\frac{\text{Gr}_C}{\text{Re}^2}\sin(\alpha)\phi^k + \frac{\chi_1}{\text{We}}\frac{1}{2}\left[3(R\bar{K})^k\frac{\partial(\phi_{\text{oil}})^k}{\partial\bar{z}} - (R\bar{K})^{k-1}\frac{\partial(\phi_{\text{oil}})^{k-1}}{\partial\bar{z}}\right] \tag{37}$$

$$\frac{\Theta^{k+1}-\Theta^k}{\Delta\bar{t}} + \frac{1}{2}\left(3u^k\frac{\partial\Theta^k}{\partial\bar{r}} - u^{k-1}\frac{\partial\Theta^{k-1}}{\partial\bar{r}}\right) + \frac{1}{2}\left(3v^k\frac{\partial\Theta^k}{\partial\bar{z}} - v^{k-1}\frac{\partial\Theta^{k-1}}{\partial\bar{z}}\right)$$

$$= \frac{\chi_5}{\text{Pe}}\left[\frac{1}{2}\left(\frac{\partial^2\Theta^{k+1}}{\partial\bar{r}^2} + \frac{\partial^2\Theta^k}{\partial\bar{r}^2}\right) + \frac{1}{\bar{r}}\frac{1}{2}\left(\frac{\partial\Theta^{k+1}}{\partial\bar{r}} + \frac{\partial\Theta^k}{\partial\bar{r}}\right)\right.$$

$$\left. + \frac{1}{2}\left(\frac{\partial^2\Theta^{k+1}}{\partial\bar{z}^2} + \frac{\partial^2\Theta^k}{\partial\bar{z}^2}\right)\right] + \chi_7\frac{\text{Ec}}{\text{Re}}\frac{1}{2}\left\{3\left[2\left(\frac{\partial u^k}{\partial\bar{r}}\right)^2 + 2\left(\frac{u^k}{\bar{r}}\right)^2 + 2\left(\frac{\partial v^k}{\partial\bar{z}}\right)^2\right.\right.$$

$$\left. + \left(\frac{\partial v^k}{\partial\bar{r}} + \frac{\partial u^k}{\partial\bar{z}}\right)^2\right] - \left[2\left(\frac{\partial u^{k-1}}{\partial\bar{r}}\right)^2 + 2\left(\frac{u^{k-1}}{\bar{r}}\right)^2 + 2\left(\frac{\partial v^{k-1}}{\partial\bar{z}}\right)^2\right.$$

$$\left.\left. + \left(\frac{\partial v^{k-1}}{\partial\bar{r}} + \frac{\partial u^{k-1}}{\partial\bar{z}}\right)^2\right]\right\} - \text{St}\frac{\chi_6}{\bar{d}}\frac{1}{2}\left(\Theta^{k+1}+\Theta^k\right) \tag{38}$$

$$\frac{\phi^{k+1}-\phi^k}{\Delta\bar{t}} + \frac{1}{2}\left(3u^k\frac{\partial\phi^k}{\partial\bar{r}} - u^{k-1}\frac{\partial\phi^{k-1}}{\partial\bar{r}}\right) + \frac{1}{2}\left(3v^k\frac{\partial\phi^k}{\partial\bar{z}} - v^{k-1}\frac{\partial\phi^{k-1}}{\partial\bar{z}}\right)$$

$$= \varepsilon_p\left\{\frac{3}{2}\left[\left[1-(\alpha_m)^k\right]\left(\phi^k - (\bar{C}_d)^k\right)\left(\frac{\partial^2 v^k}{\partial\bar{r}^2} + \frac{1}{\bar{r}}\frac{\partial v^k}{\partial\bar{r}}\right) + \left\{\left[1-(\alpha_m)^k\right]\left(\frac{\partial\phi^k}{\partial\bar{r}}\right.\right.\right.\right.$$

$$\left.\left.\left. - \left(\frac{d\bar{C}_d}{d\Theta}\right)^k\frac{\partial\Theta^k}{\partial\bar{r}}\right) - \left(\phi^k - (\bar{C}_d)^k\right)\frac{\partial(\alpha_m)^k}{\partial\bar{r}}\right\}\frac{\partial v^k}{\partial\bar{r}}\right]$$

$$- \frac{1}{2}\left[\left(1-(\alpha_m)^{k-1}\right)\left(\phi^{k-1} - (\bar{C}_d)^{k-1}\right)\right.$$

$$\left(\frac{\partial^2 v^{k-1}}{\partial\bar{r}^2} + \frac{1}{\bar{r}}\frac{\partial v^{k-1}}{\partial\bar{r}}\right) + \left\{\left(1-(\alpha_m)^{k-1}\right)\left(\frac{\partial\phi^{k-1}}{\partial\bar{r}}\right.\right.$$

$$-\left(\frac{d\bar{C}_{\mathrm{d}}}{d\Theta}\right)^{k-1}\frac{\partial\Theta^{k-1}}{\partial\bar{r}}\right)-\left(\phi^{k-1}-(\bar{C}_{\mathrm{d}})^{k-1}\right)\frac{\partial(\alpha_{\mathrm{m}})^{k-1}}{\partial\bar{r}}\right\}\frac{\partial v^{k-1}}{\partial\bar{r}}\right]\right\}$$

$$+\frac{1}{\mathrm{Re}\cdot\mathrm{Sc}}\left\{\frac{3}{2}\left[\left(\frac{d\bar{C}_{\mathrm{d}}}{d\Theta}\right)^{k}\left(\frac{\partial^2\Theta^k}{\partial\bar{r}^2}+\frac{1}{\bar{r}}\frac{\partial\Theta^k}{\partial\bar{r}}+\frac{\partial^2\Theta^k}{\partial\bar{z}^2}\right)\right.\right.$$

$$+\left(\frac{d^2\bar{C}_{\mathrm{d}}}{d\Theta^2}\right)^{k}\left\{\left(\frac{\partial\Theta^k}{\partial\bar{r}}\right)^2+\left(\frac{\partial\Theta^k}{\partial\bar{z}}\right)^2\right\}\right]$$

$$-\frac{1}{2}\left[\left(\frac{d\bar{C}_{\mathrm{d}}}{d\Theta}\right)^{k-1}\left(\frac{\partial^2\Theta^{k-1}}{\partial\bar{r}^2}+\frac{1}{\bar{r}}\frac{\partial\Theta^{k-1}}{\partial\bar{r}}+\frac{\partial^2\Theta^{k-1}}{\partial\bar{z}^2}\right)\right.$$

$$+\left.\left.\left(\frac{d^2\bar{C}_{\mathrm{d}}}{d\Theta^2}\right)^{k-1}\left\{\left(\frac{\partial\Theta^{k-1}}{\partial\bar{r}}\right)^2+\left(\frac{\partial\Theta^{k-1}}{\partial\bar{z}}\right)^2\right\}\right]\right]\right\}\tag{39}$$

$$\frac{(\alpha_{\mathrm{m}})^{k+1}-(\alpha_{\mathrm{m}})^k}{\Delta\bar{t}}+\frac{1}{2}\left(3u^k\frac{\partial(\alpha_{\mathrm{m}})^k}{\partial\bar{r}}\right.$$

$$-u^{k-1}\frac{\partial(\alpha_{\mathrm{m}})^{k-1}}{\partial\bar{r}}\right)+\frac{1}{2}\left(3v^k\frac{\partial(\alpha_{\mathrm{m}})^k}{\partial\bar{z}}-v^{k-1}\frac{\partial(\alpha_{\mathrm{m}})^{k-1}}{\partial\bar{z}}\right)$$

$$=-\frac{\mathrm{Re}}{\chi_2}\frac{1}{2}\left[3\,(\alpha_{\mathrm{m}})^k\left(\frac{\partial v^k}{\partial\bar{r}}\right)^2(\bar{K}_2)^k-(\alpha_{\mathrm{m}})^{k-1}\left(\frac{\partial v^{k-1}}{\partial\bar{r}}\right)^2(\bar{K}_2)^{k-1}\right]$$

$$+\frac{1}{2}\left[3\left[1-(\alpha_{\mathrm{m}})^k\right](\bar{K}_1)^k-\left(1-(\alpha_{\mathrm{m}})^{k-1}\right)(\bar{K}_1)^{k-1}\right]\tag{40}$$

$$\frac{(\phi_{\mathrm{oil}})^{k+1}-(\phi_{\mathrm{oil}})^k}{\Delta\bar{t}}+\frac{1}{2}\left(3u^k\frac{\partial(\phi_{\mathrm{oil}})^k}{\partial\bar{r}}-u^{k-1}\frac{\partial(\phi_{\mathrm{oil}})^{k-1}}{\partial\bar{r}}\right)$$

$$+\frac{1}{2}\left(3v^k\frac{\partial(\phi_{\mathrm{oil}})^k}{\partial\bar{z}}-v^{k-1}\frac{\partial(\phi_{\mathrm{oil}})^{k-1}}{\partial\bar{z}}\right)=0\tag{41}$$

$$\frac{\bar{\delta}^{k+1}-\bar{\delta}^k}{\Delta\bar{t}}=\frac{3}{2}\phi_1\frac{(1-f(x^k))}{x^k}\left(\frac{1}{\mathrm{Re}\cdot\mathrm{Sc}}\left(\frac{d\bar{C}_{\mathrm{d}}}{d\Theta}\right)^k\frac{\partial\Theta^k}{\partial\bar{r}}\bigg|_{\bar{r}=\bar{R}_{\mathrm{eff}}}\right)$$

$$-\frac{1}{2}\phi_1\frac{(1-f(x^{k-1}))}{x^{k-1}}\left(\frac{1}{\mathrm{Re}\cdot\mathrm{Sc}}\left(\frac{d\bar{C}_{\mathrm{d}}}{d\Theta}\right)^{k-1}\frac{\partial\Theta^{k-1}}{\partial\bar{r}}\bigg|_{\bar{r}=\bar{R}_{\mathrm{eff}}}\right)\tag{42}$$

$$\frac{x^{k+1}-x^k}{\Delta\bar{t}}=\frac{3}{2}\phi_1 f(x^k)\frac{2\left(1-\bar{\delta}^k\right)}{\bar{\delta}^k\left(2-\bar{\delta}^k\right)}\left[\frac{1}{\mathrm{Re}\cdot\mathrm{Sc}}\left(\frac{d\bar{C}_{\mathrm{d}}}{d\Theta}\right)^k\right.$$

$$\frac{\partial\Theta^k}{\partial\bar{r}}+\varepsilon_{\mathrm{p}}\left[1-(\alpha_{\mathrm{m}})^k\right]\left(\phi^k-(\bar{C}_{\mathrm{d}})^k\right)\frac{\partial v^k}{\partial\bar{r}}\bigg]_{\bar{r}=\bar{R}_{\mathrm{eff}}}$$

$$-\frac{1}{2}\phi_1 f(x^{k-1})\frac{2\left(1-\bar{\delta}^{k-1}\right)}{\bar{\delta}^{k-1}\left(2-\bar{\delta}^{k-1}\right)}\left[\frac{1}{\mathrm{Re}\cdot\mathrm{Sc}}\left(\frac{d\bar{C}_{\mathrm{d}}}{d\Theta}\right)^{k-1}\frac{\partial\Theta^{k-1}}{\partial\bar{r}}+\varepsilon_{\mathrm{p}}\left(1-(\alpha_{\mathrm{m}})^{k-1}\right)\right.$$

$$\left(\phi^{k-1}-(\bar{C}_{\mathrm{d}})^{k-1}\right)\frac{\partial v^{k-1}}{\partial\bar{r}}\bigg]_{\bar{r}=\bar{R}_{\mathrm{eff}}}.\tag{43}$$

The arbitrary functions $f(x^{k-1})$ and $f(x^k)$ are given by

$$f(x^{k-1}) = \frac{1 - x^{k-1}}{\alpha_{\text{avg}}^2 (x^{k-1})^2 - x^{k-1} + 1} \tag{44}$$

$$f(x^k) = \frac{1 - x^k}{\alpha_{\text{avg}}^2 (x^k)^2 - x^k + 1} \tag{45}$$

The intermediate functions u^k, v^k, P^k, Θ^k, ϕ^k, $(\alpha_{\text{m}})^k$, $(\phi_{\text{oil}})^k$, δ^k and x^k are expanded using first-order Taylor series about the point $(\bar{r}, \bar{z}, \bar{t}_{k-1})$ to get:

$$u^k = u^{k-1} + \Delta\bar{t}\Bigg\{ - u^{k-1}\frac{\partial u^{k-1}}{\partial\bar{r}} - v^{k-1}\frac{\partial u^{k-1}}{\partial\bar{z}}$$

$$- \frac{\partial P^{k-1}}{\partial\bar{r}} - \frac{\chi_2}{(\text{Re}\cdot\text{Da})}u^{k-1} + \frac{\chi_2}{\text{Re}}\Bigg(2\frac{\partial^2 u^{k-1}}{\partial\bar{r}^2}$$

$$+ \frac{\partial^2 u^{k-1}}{\partial\bar{z}^2} + \frac{\partial^2 v^{k-1}}{\partial\bar{r}\partial\bar{z}} + \frac{2}{\bar{r}}\frac{\partial u^{k-1}}{\partial\bar{r}} - \frac{2}{\bar{r}^2}u^{k-1}\Bigg)$$

$$+ \chi_3\frac{\text{Gr}_T}{\text{Re}^2}\cos(\alpha)\Theta^{k-1} + \chi_4\frac{\text{Gr}_C}{\text{Re}^2}\cos(\alpha)\phi^{k-1}$$

$$+ \frac{\chi_1}{\text{We}}(R\bar{K})^{k-1}\frac{\partial(\phi_{\text{oil}})^{k-1}}{\partial\bar{r}} \Bigg\} \tag{46}$$

$$v^k = v^{k-1} + \Delta\bar{t}\Bigg\{ - u^{k-1}\frac{\partial v^{k-1}}{\partial\bar{r}} - v^{k-1}\frac{\partial v^{k-1}}{\partial\bar{z}}$$

$$- \frac{\partial P^{k-1}}{\partial\bar{z}} - \frac{\chi_2}{(\text{Re}\cdot\text{Da})}v^{k-1} + \frac{\chi_2}{\text{Re}}\Bigg(\frac{\partial^2 v^{k-1}}{\partial\bar{r}^2}$$

$$+ 2\frac{\partial^2 v^{k-1}}{\partial\bar{z}^2} + \frac{\partial^2 u^{k-1}}{\partial\bar{r}\partial\bar{z}} + \frac{1}{\bar{r}}\frac{\partial u^{k-1}}{\partial\bar{z}} + \frac{1}{\bar{r}}\frac{\partial v^{k-1}}{\partial\bar{r}}\Bigg)$$

$$+ \chi_3\frac{\text{Gr}_T}{\text{Re}^2}\sin(\alpha)\Theta^{k-1} + \chi_4\frac{\text{Gr}_C}{\text{Re}^2}\sin(\alpha)\phi^{k-1}$$

$$+ \frac{\chi_1}{\text{We}}(R\bar{K})^{k-1}\frac{\partial(\phi_{\text{oil}})^{k-1}}{\partial\bar{z}} \Bigg\} \tag{47}$$

$$\Theta^k = \Theta^{k-1} + \Delta\bar{t}\Bigg\{ - u^{k-1}\frac{\partial\Theta^{k-1}}{\partial\bar{r}} - v^{k-1}\frac{\partial\Theta^{k-1}}{\partial\bar{z}}$$

$$+ \frac{\chi_5}{\text{Pe}}\Bigg(\frac{\partial^2\Theta^{k-1}}{\partial\bar{r}^2} + \frac{1}{\bar{r}}\frac{\partial\Theta^{k-1}}{\partial\bar{r}} + \frac{\partial^2\Theta^{k-1}}{\partial\bar{z}^2}\Bigg)$$

$$- \text{St}\frac{\chi_6}{\bar{d}}\Theta^{k-1} + \chi_7\frac{\text{Ec}}{\text{Re}}\Bigg[2\Bigg(\frac{\partial u^{k-1}}{\partial\bar{r}}\Bigg)^2 + 2\Bigg(\frac{u^{k-1}}{\bar{r}}\Bigg)^2$$

$$+ 2\Bigg(\frac{\partial v^{k-1}}{\partial\bar{z}}\Bigg)^2 + \Bigg(\frac{\partial v^{k-1}}{\partial\bar{r}} + \frac{\partial u^{k-1}}{\partial\bar{z}}\Bigg)^2\Bigg]\Bigg\} \tag{48}$$

$$\phi^k = \phi^{k-1} + \Delta\bar{t}\Bigg\{ - u^{k-1}\frac{\partial\phi^{k-1}}{\partial\bar{r}} - v^{k-1}\frac{\partial\phi^{k-1}}{\partial\bar{z}}$$

$$+ \varepsilon_{\text{p}}\Bigg[\Big[1 - (\alpha_{\text{m}})^{k-1}\Big]\Big[\phi^{k-1} - (\bar{C}_{\text{d}})^{k-1}\Big]$$

$$* \left(\frac{\partial^2 v^{k-1}}{\partial \bar{r}^2} + \frac{1}{\bar{r}} \frac{\partial v^{k-1}}{\partial \bar{r}} \right) + \left\{ \left[1 - (\alpha_m)^{k-1} \right] \right.$$

$$* \left(\frac{\partial \phi^{k-1}}{\partial \bar{r}} - \left(\frac{d\bar{C}_d}{d\Theta} \right)^{k-1} \frac{\partial \Theta^{k-1}}{\partial \bar{r}} \right)$$

$$- \left(\phi^{k-1} - (\bar{C}_d)^{k-1} \right) \frac{\partial (\alpha_m)^{k-1}}{\partial \bar{r}} \left. \right\} \frac{\partial v^{k-1}}{\partial \bar{r}} \right]$$

$$+ \frac{1}{\mathrm{Re} \cdot \mathrm{Sc}} \left[\left(\frac{d\bar{C}_d}{d\Theta} \right)^{k-1} \left(\frac{\partial^2 \Theta^{k-1}}{\partial \bar{r}^2} + \frac{1}{\bar{r}} \frac{\partial \Theta^{k-1}}{\partial \bar{r}} \right. \right.$$

$$\left. + \frac{\partial^2 \Theta^{k-1}}{\partial \bar{z}^2} \right) + \left(\frac{d^2 \bar{C}_d}{d\Theta^2} \right)^{k-1}$$

$$\left. * \left\{ \left(\frac{\partial \Theta^{k-1}}{\partial \bar{r}} \right)^2 + \left(\frac{\partial \Theta^{k-1}}{\partial \bar{z}} \right)^2 \right\} \right] \right\} \tag{49}$$

$$(\alpha_m)^k = (\alpha_m)^{k-1} + \Delta \bar{t} \left\{ - u^{k-1} \frac{\partial (\alpha_m)^{k-1}}{\partial \bar{r}} \right.$$

$$- v^{k-1} \frac{\partial (\alpha_m)^{k-1}}{\partial \bar{z}} + \left[1 - (\alpha_m)^{k-1} \right] (\bar{K}_1)^{k-1}$$

$$\left. - \frac{\mathrm{Re}}{\chi_2} (\alpha_m)^{k-1} \left(\frac{\partial v^{k-1}}{\partial \bar{r}} \right)^2 (\bar{K}_2)^{k-1} \right\} \tag{50}$$

$$(\phi_{\mathrm{oil}})^k = (\phi_{\mathrm{oil}})^{k-1} + \Delta \bar{t} \left\{ - u^{k-1} \frac{\partial (\phi_{\mathrm{oil}})^{k-1}}{\partial \bar{r}} \right.$$

$$\left. - v^{k-1} \frac{\partial (\phi_{\mathrm{oil}})^{k-1}}{\partial \bar{z}} \right\} \tag{51}$$

$$\bar{\delta}^k = \bar{\delta}^{k-1} + \Delta \bar{t} \left\{ \phi_1 \frac{(1 - f(x^{k-1}))}{x^{k-1}} \right.$$

$$\left. * \left(\frac{1}{\mathrm{Re} \cdot \mathrm{Sc}} \left(\frac{d\bar{C}_d}{d\Theta} \right)^{k-1} \frac{\partial \Theta^{k-1}}{\partial \bar{r}} \bigg|_{\bar{r} = \bar{R}_{\mathrm{eff}}} \right) \right\} \tag{52}$$

$$x^k = x^{k-1} + \Delta \bar{t} \left\{ \phi_1 f(x^{k-1}) \frac{2 \left(1 - \bar{\delta}^{k-1} \right)}{\bar{\delta}^{k-1} \left(2 - \bar{\delta}^{k-1} \right)} \right.$$

$$* \left[\frac{1}{\mathrm{Re} \cdot \mathrm{Sc}} \left(\frac{d\bar{C}_d}{d\Theta} \right)^{k-1} \frac{\partial \Theta^{k-1}}{\partial \bar{r}} + \varepsilon_p \left(1 - (\alpha_m)^{k-1} \right) \right.$$

$$\left. * \left(\phi^{k-1} - (\bar{C}_d)^{k-1} \right) \frac{\partial v^{k-1}}{\partial \bar{r}} \right]_{\bar{r} = \bar{R}_{\mathrm{eff}}} \right\} \tag{53}$$

The time-discretized initial and boundary conditions are given as follows:

$$u_{\bar{r}}^{k+1}(0, \bar{z}) = 0, \ v_{\bar{r}}^{k+1}(0, \bar{z}) = 0, \ \Theta_{\bar{r}}^{k+1}(0, \bar{z}) = 0,$$
$$\phi_{\bar{r}}^{k+1}(0, \bar{z}) = 0, \ \alpha_{m\bar{r}}^{k+1}(0, \bar{z}) = 0, \ \phi_{\mathrm{oil}\bar{r}}^{k+1}(0, \bar{z}) = 0 \tag{54}$$

$$u^{k+1}(1, \bar{z}) = 0, \ v^{k+1}(1, \bar{z}) = 0, \ \Theta^{k+1}(1, \bar{z}) = 1,$$
$$\phi^{k+1}(1, \bar{z}) = 1. \tag{55}$$

$$u^{k+1}(\bar{r}, 0) = 0, \ v^{k+1}(\bar{r}, 0) = 1, \ \Theta^{k+1}(\bar{r}, 0) = 0,$$
$$\phi^{k+1}(\bar{r}, 0) = 0, \ (\alpha_{\mathrm{m}})^{k+1}(\bar{r}, 0) = 0, \tag{56}$$
$$(\phi_{\mathrm{oil}})^{k+1}(\bar{r}, 0) = 1 - \phi_{\mathrm{water}}$$

$$u_{\bar{z}}^{k+1}(\bar{r}, L) = 0, \ v_{\bar{z}}^{k+1}(\bar{r}, L) = 0, \ \Theta_{\bar{z}}^{k+1}(\bar{r}, L) = 0,$$
$$\phi_{\bar{z}}^{k+1}(\bar{r}, L) = 0, \ \alpha_{\mathrm{m}\bar{z}}^{\ k+1}(\bar{r}, L) = 0, \ \phi_{\mathrm{oil}\bar{z}}^{\ k+1}(\bar{r}, L) = 0 \tag{57}$$

$$u^0(\bar{r}, \bar{z}) = 0, \ v^0(\bar{r}, \bar{z}) = 0, \ P^0(\bar{r}, \bar{z}) = 0,$$
$$\Theta^0(\bar{r}, \bar{z}) = 0, \ \phi^0(\bar{r}, \bar{z}) = 0, \ \alpha_{\mathrm{m}}^0(\bar{r}, \bar{z}) = 0, \tag{58}$$
$$\phi_{\mathrm{oil}}^0(\bar{r}, \bar{z}) = 1 - \phi_{\mathrm{water}}, \ \bar{\delta}^0 = 0, \ x^0 = 0$$

The linear iterative schemes (36)−(53) and the corresponding initial boundary conditions (54)−(58) are discrete-in-time and continuous-in-space.

Spatial Discretization

The linear iterative schemes (36)−(53) are discretized in space using the bivariate Chebyshev spectral collocation method [27]. The domain $\bar{r} \in [\bar{r}_0, \bar{r}_\infty]$ is transformed to the new domain $\hat{r} \in [-1, 1]$ using the linear transformation

$$\bar{r} = \frac{1}{2}(\bar{r}_\infty - \bar{r}_0)\hat{r} + \frac{1}{2}(\bar{r}_\infty + \bar{r}_0) \tag{59}$$

The domain $\bar{z} \in [\bar{z}_0, \bar{z}_\infty]$ is transformed to the new domain $\hat{z} \in [-1, 1]$ using the linear transformation

$$\bar{z} = \frac{1}{2}(\bar{z}_\infty - \bar{z}_0)\hat{z} + \frac{1}{2}(\bar{z}_\infty + \bar{z}_0). \tag{60}$$

Lagrange fundamentals (or Lagrange coefficients) are chosen as the basis functions. We use the bivariate Lagrange interpolating polynomials to approximate the unknown functions $u(\bar{r}, \bar{z}, \bar{t}_{k+1}), v(\bar{r}, \bar{z}, \bar{t}_{k+1}), \Theta(\bar{r}, \bar{z}, \bar{t}_{k+1}), \phi(\bar{r}, \bar{z}, \bar{t}_{k+1}), \alpha_{\mathrm{m}}(\bar{r}, \bar{z}, \bar{t}_{k+1})$, and $\phi_{\mathrm{oil}}(\bar{r}, \bar{z}, \bar{t}_{k+1})$:

$$u(\bar{r}, \bar{z}, \bar{t}_{k+1}) \approx \sum_{m=0}^{M} \sum_{n=0}^{N} u(\hat{r}_m, \hat{z}_n, \bar{t}_{k+1}) L_m(\hat{r}) L_n(\hat{z}) \tag{61}$$

$$v(\bar{r}, \bar{z}, \bar{t}_{k+1}) \approx \sum_{m=0}^{M} \sum_{n=0}^{N} v(\hat{r}_m, \hat{z}_n, \bar{t}_{k+1}) L_m(\hat{r}) L_n(\hat{z}) \tag{62}$$

$$\Theta(\bar{r}, \bar{z}, \bar{t}_{k+1}) \approx \sum_{m=0}^{M} \sum_{n=0}^{N} \Theta(\hat{r}_m, \hat{z}_n, \bar{t}_{k+1}) L_m(\hat{r}) L_n(\hat{z}) \tag{63}$$

$$\phi(\bar{r}, \bar{z}, \bar{t}_{k+1}) \approx \sum_{m=0}^{M} \sum_{n=0}^{N} \phi(\hat{r}_m, \hat{z}_n, \bar{t}_{k+1}) L_m(\hat{r}) L_n(\hat{z}) \tag{64}$$

$$\alpha_{\mathrm{m}}(\bar{r}, \bar{z}, \bar{t}_{k+1}) \approx \sum_{m=0}^{M} \sum_{n=0}^{N} \alpha_{\mathrm{m}}(\hat{r}_m, \hat{z}_n, \bar{t}_{k+1}) L_m(\hat{r}) L_n(\hat{z}) \tag{65}$$

$$\phi_{\mathrm{oil}}(\bar{r}, \bar{z}, \bar{t}_{k+1}) \approx \sum_{m=0}^{M} \sum_{n=0}^{N} \phi_{\mathrm{oil}}(\hat{r}_m, \hat{z}_n, \bar{t}_{k+1}) L_m(\hat{r}) L_n(\hat{z}) \tag{66}$$

The Lagrange cardinal polynomials are defined by

$$
L_m(\hat{r}) = \prod_{\substack{i=0 \\ i \neq m}}^{M} \frac{(\hat{r} - \hat{r}_i)}{(\hat{r}_m - \hat{r}_i)}; \quad L_m(\hat{r}_i) = \delta_{mi} = \begin{cases} 1, & \text{if } i = m \\ 0, & \text{if } i \neq m \end{cases} \tag{67}
$$

$$
L_n(\hat{z}) = \prod_{\substack{j=0 \\ j \neq n}}^{N} \frac{(\hat{z} - \hat{z}_j)}{(\hat{z}_n - \hat{z}_j)}; \quad L_n(\hat{z}_j) = \delta_{nj} = \begin{cases} 1, & \text{if } j = n \\ 0, & \text{if } j \neq n. \end{cases} \tag{68}
$$

The above interpolations utilize symmetrically distributed Chebyshev-Gauss-Lobatto grid points $(\hat{r}_i, \hat{z}_j)$ defined on the domain $[-1, 1] \times [-1, 1]$ by:

$$
\hat{r}_i = \cos\left(\frac{\pi i}{M}\right) \quad \text{and} \quad \hat{z}_j = \cos\left(\frac{\pi j}{N}\right) \tag{69}
$$

for $i = 0, 1, \cdots, M$; $j = 0, 1, \cdots, N$ where M and N denote the number of collocation (or grid) points in $\bar{r}$ and $\bar{z}$ direction, respectively.

The Chebyshev-Gauss-Lobatto grid points are chosen to transform the continuous spatial derivatives (in both $\bar{r}$ and $\bar{z}$) to discrete matrix form at the collocation points using standard Chebyshev derivative matrices $[D_{i,m}]$ and $[d_{j,n}]$ [28], as illustrated below:

$$
\begin{aligned}
\left.\frac{\partial u}{\partial \bar{r}}\right|_{(\bar{r}_i, \bar{z}_j)} &\approx \sum_{m=0}^{M} \sum_{n=0}^{N} u(\hat{r}_m, \hat{z}_n, \bar{t}_{k+1}) L_n(\hat{z}_j) \left(\frac{\mathrm{d}L_m(\hat{r})}{\mathrm{d}\hat{r}} \frac{\mathrm{d}\hat{r}}{\mathrm{d}\bar{r}}\right)\Bigg|_{\hat{r}=\hat{r}_i} \\
&= \mathbf{D}\mathbf{U}_j^{(k+1)}, \text{ at } \bar{z} = \bar{z}_j \text{ and } \bar{t} = \bar{t}_{k+1}
\end{aligned} \tag{70}
$$

$$
\begin{aligned}
\left.\frac{\partial u}{\partial \hat{z}}\right|_{(\bar{r}_i, \bar{z}_j)} &\approx \sum_{m=0}^{M} \sum_{n=0}^{N} u(\hat{r}_m, \hat{z}_n, \bar{t}_{k+1}) L_m(\hat{r}_i) \left(\frac{\mathrm{d}L_n(\hat{z})}{\mathrm{d}\hat{z}} \frac{\mathrm{d}\hat{z}}{\mathrm{d}\bar{z}}\right)\Bigg|_{\hat{z}=\hat{z}_j} \\
&= \sum_{n=0}^{N} \mathbf{d}_{j,n} \mathbf{U}_n^{(k+1)}
\end{aligned} \tag{71}
$$

$$
\left.\frac{\partial^2 u}{\partial \bar{r}^2}\right|_{(\bar{r}_i, \bar{z}_j)} \approx \mathbf{D}^2 \mathbf{U}_j^{(k+1)}, \tag{72}
$$

$$
\left.\frac{\partial^2 u}{\partial \bar{z}^2}\right|_{(\bar{r}_i, \bar{z}_j)} \approx \sum_{n=0}^{N} \mathbf{d}_{j,n}^2 \mathbf{U}_n^{(k+1)} \tag{73}
$$

$$
\left.\frac{\partial^2 u}{\partial \bar{r} \partial \bar{z}}\right|_{(\bar{r}_i, \bar{z}_j)} \approx \sum_{n=0}^{N} \mathbf{d}_{j,n} \mathbf{D}\mathbf{U}_n^{(k+1)}, \tag{74}
$$

where

$$
\mathbf{D} = [2/(\bar{r}_\infty - \bar{r}_0)][D_{i,m}], \text{ for } i, m = 0, 1, 2, \cdots, M
$$
$$
\mathbf{U}_j^{(k+1)} = [u(\bar{r}_0, \bar{z}_j, \bar{t}_{k+1}), u(\bar{r}_1, \bar{z}_j, \bar{t}_{k+1}), \cdots, u(\bar{r}_M, \bar{z}_j, \bar{t}_{k+1})]^{\mathrm{T}}
$$
$$
\mathbf{d} = [2/(\bar{z}_\infty - \bar{z}_0)][d_{j,n}], \text{ for } j, n = 0, 1, 2, \cdots, N.
$$

The partial derivatives of the other dependent variables, i.e., $v(\bar{r}, \bar{z}, \bar{t}_{k+1})$, $\Theta(\bar{r}, \bar{z}, \bar{t}_{k+1})$, $\phi(\bar{r}, \bar{z}, \bar{t}_{k+1})$, $\alpha_\mathrm{m}(\bar{r}, \bar{z}, \bar{t}_{k+1})$, and $\phi_\mathrm{oil}(\bar{r}, \bar{z}, \bar{t}_{k+1})$, with respect to $\bar{r}$ and $\bar{z}$ are similarly transformed to discrete matrix form. We remark that the grid points are indexed from right to left in the $\bar{r}$ and $\bar{z}$ domain. So $\bar{z} = 0$ corresponds to the collocation point $\hat{z}_N$.

Fig. 3 Temporal evolution of the axial velocity
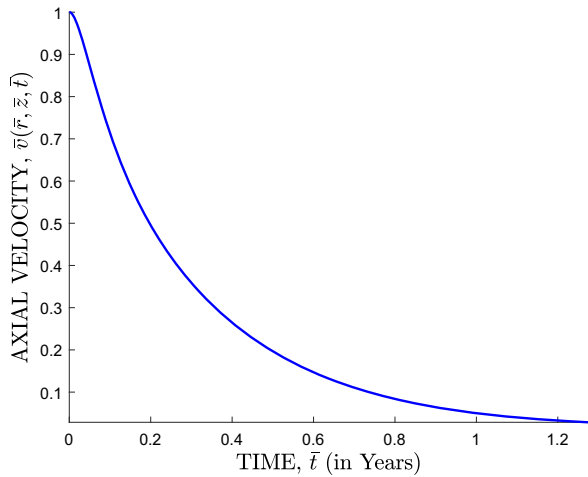
Substituting the respective discrete derivative matrices into the temporal schemes above yields matrix systems of the form

$$\mathbf{AU} = \mathbf{R}, \tag{75}$$

where $\mathbf{A}$ is the coefficient matrix, $\mathbf{U}$ is the unknown column vector, and $\mathbf{R}$ is the solution matrix. The corresponding boundary conditions are imposed on the main diagonal of the subblock matrices of $\mathbf{A}$.

The system (75) is solved starting from suitable initial guesses. The iteration is repeated for $k = 1, 2, 3, \cdots$, until the prescribed absolute error tolerance is reached. MATLAB® software is utilized for the computer simulations.

Results and Discussion

The flow variables investigated in this study are axial (streamwise) velocity, radial velocity, fluid temperature, total wax concentration, wax aggregation degree, oil volume fraction, wax deposit thickness, and weight fraction of wax molecules in the gel layer.

Temporal Evolution of the Flow Variables

In this section, the flow variables are plotted against time to analyze their temporal evolution. The results are presented in the form of graphs, which are carefully examined and discussed.

It is observed in Fig. 3 that the axial velocity profile of waxy crude oil decreases with an increase in time. This is attributed to the gradual accumulation of wax crystals on the pipe walls, which constricts the flow path and reduces the effective cross-sectional area of the pipeline. This constriction effectively reduces the overall flow velocity, contributing to the decrease in axial velocity. Over time, detached wax particles may settle towards the bottom of the pipeline, further reducing the effective flow area and hindering fluid movement. Additionally, the presence of wax deposit can create a temperature gradient along the pipeline. As wax crystals accumulate, they absorb heat from the flowing crude oil, causing a tempera-

Fig. 4 Temporal evolution of the temperature
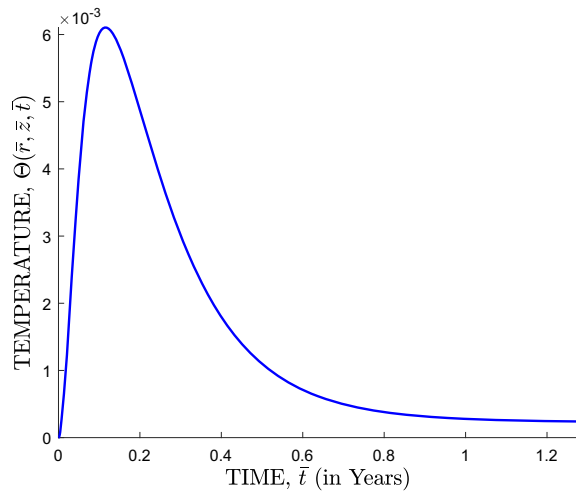
ture decrease near the wall. This temperature gradient affects the wax precipitation kinetics, potentially accelerating the deposition process and exacerbating the velocity reduction.

It is observed in Fig. 4 that the temperature profile of waxy crude oil increases sharply at first and then decreases thereafter with an increase in time. This behavior is attributed to the interplay between the heat transfer process and wax deposition. Initially, as the waxy crude oil is transported through the pipeline, heat transfer from the flowing fluid to the pipe wall occurs, causing the temperature of the waxy crude oil to increase. However, as wax crystals precipitate and accumulate on the pipe walls, they act as insulators, hindering further heat transfer from the fluid to the pipe wall. This reduced heat transfer slows down the temperature increase, and eventually, the temperature starts to decrease due to the ongoing heat losses to the environment. The wax deposition process also affects the temperature distribution within the waxy crude oil. As wax crystals form, they can trap pockets of warmer fluid, creating a temperature gradient along the pipeline. This temperature gradient can further influence the wax precipitation kinetics, potentially accelerating the deposition process and exacerbating the temperature decrease.

It is observed in Fig. 5 that the concentration profile of wax molecules in waxy crude oil increases steadily with an increase in time. This increase is attributed to the ongoing precipitation of wax crystals as the oil temperature decreases. As the temperature falls below the wax appearance temperature (WAT), the solubility of wax molecules in the oil diminishes, causing them to precipitate out of solution and form wax crystals. These newly formed wax crystals then disperse throughout the oil, leading to a gradual increase in the overall concentration of wax molecules.

It is observed in Fig. 6 that the oil volume fraction profile for waxy crude oil decreases steadily with an increase in time. This reduction is attributed to the progressive accumulation of wax crystals on the pipe walls. As wax crystals precipitate and grow, they occupy a larger volume, effectively displacing the oil and gradually reducing the overall oil volume fraction. This displacement of oil is particularly pronounced near the pipe walls, where the wax crystals preferentially accumulate due to the lower temperatures and enhanced shear rates. The reduction in oil volume fraction can have several implications for the flow behavior of waxy crude oil. For example, it can lead to the formation of unstable oil-wax interfaces.

Fig. 5 Temporal evolution of the total concentration of wax molecules
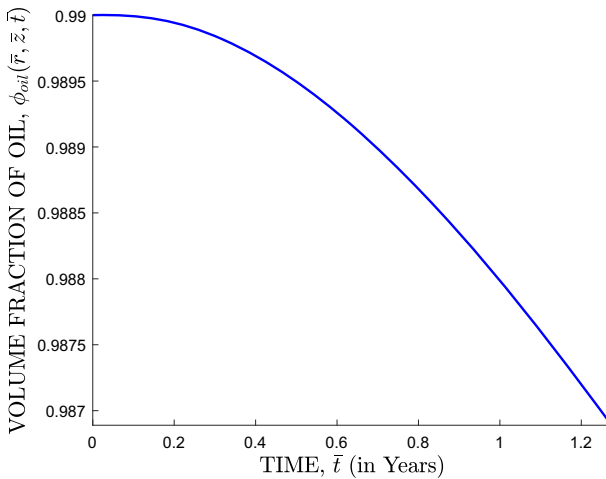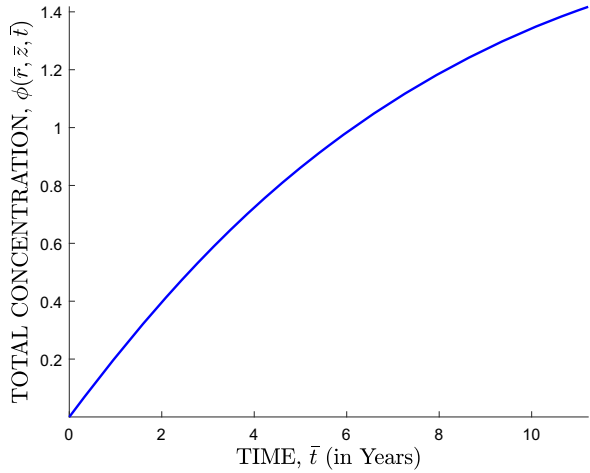

Fig. 6 Temporal evolution of the oil volume fraction

These unstable interfaces can become sites for further wax precipitation and deposition, further contributing to the potential blockage of the pipeline.

It is observed in Fig. 7 that the wax deposition thickness profile for waxy crude oil in a pipeline increases initially and then plateaus, reaching a steady-state. This behavior is attributed to the interplay between wax deposition and removal processes. Initially, as the waxy crude oil flows through the pipeline and its temperature falls below the wax appearance temperature (WAT), wax molecules precipitate from the solution and form wax crystals. These crystals accumulate on the pipe walls, leading to a gradual increase in the wax deposit thickness. The wax deposition rate is initially high due to the substantial concentration gradient between the bulk oil and the pipe wall, creating a favorable environment for crystal nucleation and growth. However, as the wax deposit thickness increases, the wax deposit acts as an insulator, impeding heat transfer from the bulk oil to the pipe wall. This reduced heat transfer slows down the wax precipitation kinetics, causing the deposition rate to decline

Fig. 7 Temporal evolution of the wax deposit thickness
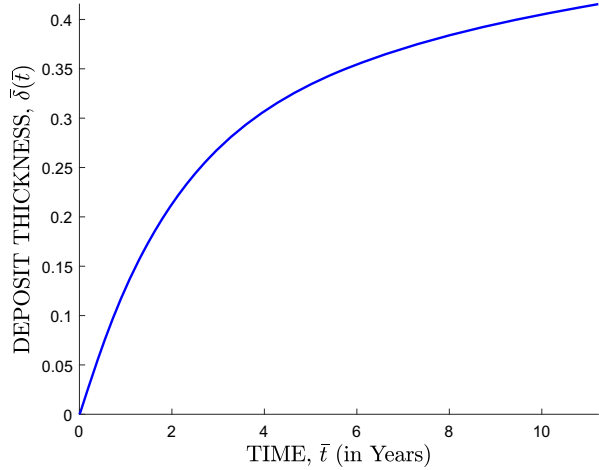
Fig. 8 Temporal evolution of the weight fraction of wax in the gel layer
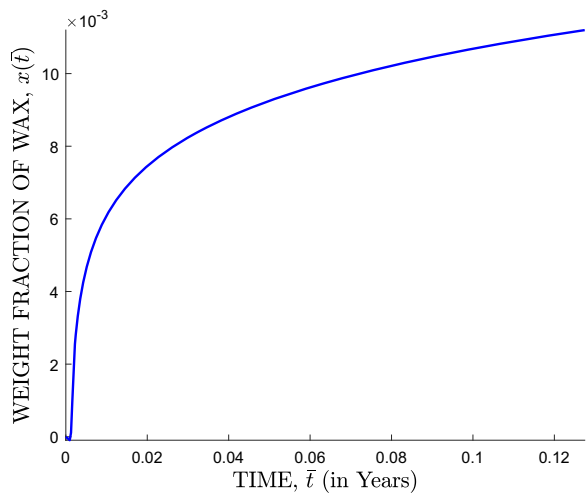
over time. Eventually, a steady-state is reached when the deposition rate is balanced by the removal rate, resulting in a stable wax deposit thickness profile.

It is observed in Fig. 8 that the weight fraction of wax crystals in the gel layer for the flow of waxy crude oil in a pipeline increases with an increase in time and then reaches a steady-state. This behavior is attributed to the interplay between wax deposition and gelation processes. Initially, as waxy crude oil flows through the pipeline, wax crystals precipitate and accumulate on the pipe walls, forming a gel layer. This gel layer gradually increases in weight fraction as more wax crystals deposit and integrate into the gel structure. However, as the weight fraction of wax crystals in the gel layer increases, the growing gel layer augments the viscosity of the oil near the pipe walls, diminishing the shear forces that can disrupt the gel structures. This reduced shear force decelerates the gelation process and impedes the further incorporation of wax crystals into the gel layer. Eventually, a steady-state is attained when the rate of wax deposition and gelation is balanced by the reduced rate of crystal incorporation and gel growth, resulting in a stable weight fraction of wax crystals in the gel layer.

Fig. 9 Effects of varying Reynolds number on the wax deposit thickness
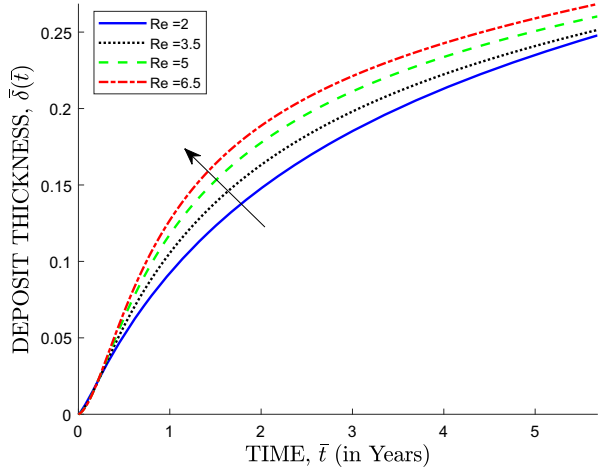
Fig. 10 Effects of varying mass Grashof number on the wax deposit thickness
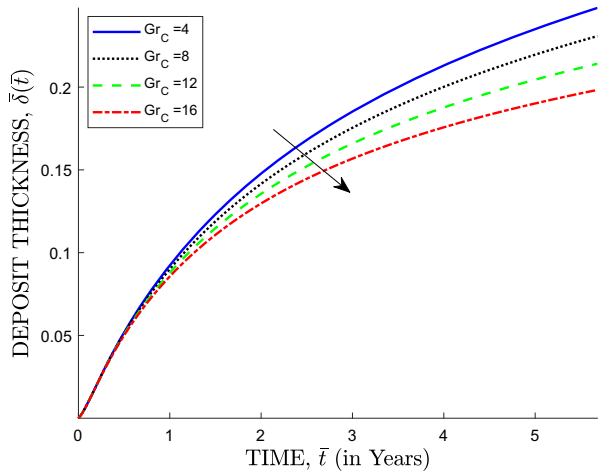
Effects of Varying Flow Parameters on the Flow Variables

In this section, the flow variables are plotted against the axial distance from the pipe inlet. The flow parameters are systematically varied one at a time within a computational framework to assess their individual effects on the flow behavior. The various flow parameters investigated include the Reynolds number (Re), mass Grashof number (Gr_C), Schmidt number (Sc), and Weber number (We). The results obtained from the parametric variations are presented in the form of graphs, and their implications are thoroughly discussed.

Wax Deposition

It is observed in Fig. 9 that an increase in the Reynolds number causes an increase in the wax deposit thickness for flow of waxy crude oil in a pipeline within the laminar flow regime. Increasing the Reynolds number implies that the inertial forces become more dominant than the viscous forces. This observed trend is attributed to the increase in shear stress at the pipe

Springer

Fig. 11 Effects of varying Schmidt number on the wax deposit thickness
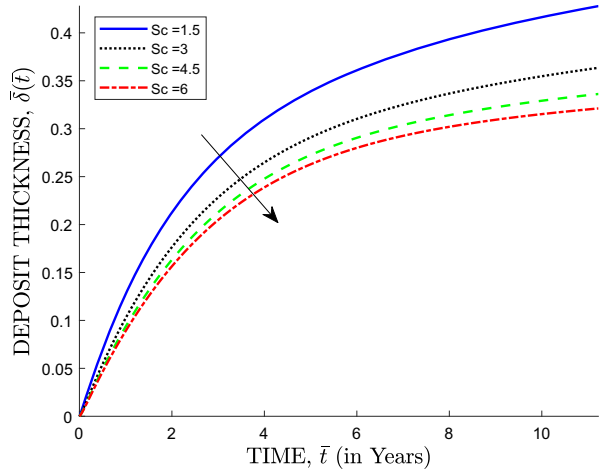
wall as the Reynolds number increases. This shear stress enhances the rate of diffusion of wax molecules from the bulk of the oil to the pipe wall. This enhancement occurs because the shear stress causes the wax molecules to move faster, which then leads to their precipitation and deposition on the pipe, consequently increasing the deposit thickness.

It is observed in Fig. 10 that an increase in the mass Grashof number causes a decrease in the thickness of wax deposit profiles for flow of waxy crude oil in a pipeline. An increase in the mass Grashof number signifies that buoyancy forces, which arise from density differences due to temperature variations, become more dominant than viscous forces, which govern the flow behavior in laminar conditions in the pipeline. The enhanced buoyancy forces lead to a more buoyant flow pattern, disrupting the diffusion of wax molecules from the bulk oil towards the pipe wall. This diffusion process is crucial for wax deposition to occur. The increased turbulence caused by buoyancy forces can re-entrain wax molecules that have already deposited on the pipe wall, preventing them from forming a thick deposit layer. The dominant buoyancy forces promote a stratified flow pattern, where the oil with the highest wax concentration is located closer to the pipe wall. This reduces the concentration gradient driving wax diffusion, further hindering deposition. The combined effects of disrupted diffusion, wax re-entrainment, and stratified flow lead to a decrease in the rate of wax deposition, resulting in thinner deposit profiles.

It is observed in Fig. 11 that an increase in the Schmidt number causes a decrease in the thickness of wax deposit profiles for flow of waxy crude oil in a pipeline. Increasing the Schmidt number implies that momentum diffusivity, which describes the rate at which wax molecules are transported by fluid motion, becomes more dominant than mass diffusivity, which describes the rate of transport of wax molecules by molecular diffusion. Thus, the observed trend is attributed to the interplay between mass transfer and wax deposition processes. As the Schmidt number increases, the mass transfer rate of wax molecules from the bulk oil to the pipe wall decreases. This reduced mass transfer rate slows down the wax deposition process, leading to a slower growth of the wax deposit layer.

It is observed in Fig. 12 that an increase in the Weber number causes a decrease in the thickness of wax deposit profiles for flow of waxy crude oil in a pipeline. Increasing the Weber number implies that inertial forces, which represent the flow stresses, become more dominant than surface tension forces, which represent the cohesive forces between wax crystals. Thus, the observed trend is attributed to the interplay between flow stresses and wax deposition

Fig. 12 Effects of varying Weber number on the wax deposit thickness
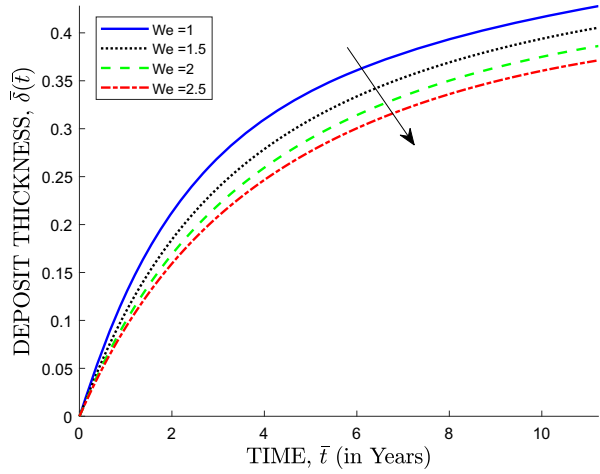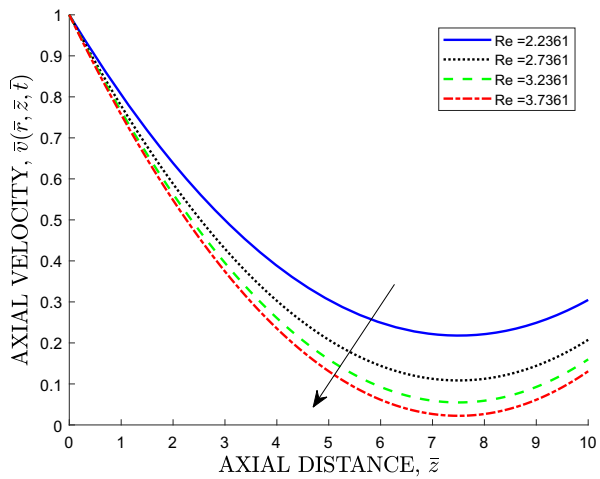

Fig. 13 Effects of varying Reynolds number on the axial velocity profiles

processes. As the Weber number increases, the flow stresses near the pipe wall intensify, leading to a more dispersed distribution of wax crystals throughout the flow cross-section. This dispersion diminishes the concentration gradient between the bulk oil and the pipe wall, making it more challenging for wax crystals to adhere to the pipe surface. Furthermore, the elevated flow stresses can act to remove wax crystals that have already deposited on the pipe walls. This mechanical removal process contributes to limiting the overall thickness of the wax deposit.

Axial Velocity of Waxy Crude Oil

It is observed in Fig. 13 that an increase in the Reynolds number causes a decrease in the axial velocity profiles for flow of waxy crude oil in a pipeline within the laminar flow regime. As the Reynolds number increases, the inertial forces acting on the fluid particles become more dominant than the viscous forces. This causes the fluid particles to move more randomly, and the axial velocity profile becomes flatter, hence leading to a decrease in axial velocity.

Fig. 14 Effects of varying mass Grashof number on the axial velocity profiles
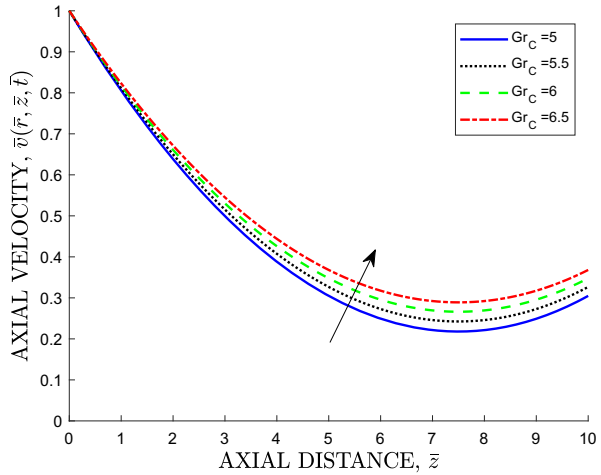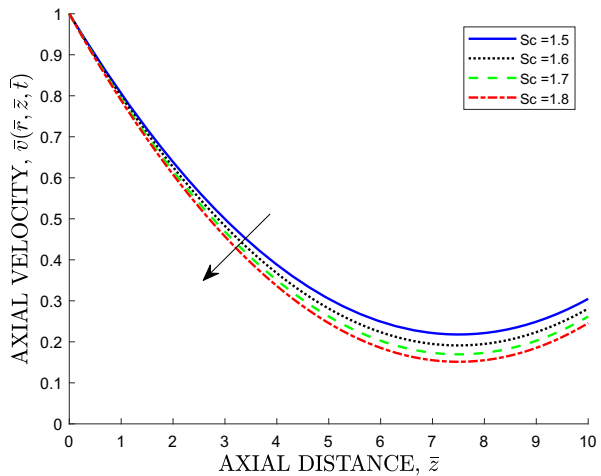

Fig. 15 Effects of varying Schmidt number on the axial velocity profiles

It is observed in Fig. 14 that an increase in the mass Grashof number leads to an increase in the axial velocity profiles for the flow of waxy crude oil in a pipeline. A higher mass Grashof number indicates that the buoyancy force acting on the fluid element is stronger relative to the viscous force opposing the fluid flow. This stronger buoyancy force causes the fluid element to accelerate more rapidly in the axial direction.

It is observed in Fig. 15 that an increase in the Schmidt number leads to a decrease in the axial velocity profiles for the flow of waxy crude oil in a pipeline. A higher Schmidt number indicates that the wax molecules can diffuse through the fluid more quickly. This enhanced diffusion allows the wax molecules to reach the pipe walls more easily, where they can deposit and form a gel-like layer. This gel-like layer grows and reduces the available flow area within the pipe, which eventually slows down the flow of the fluid in the axial direction.

It is observed in Fig. 16 that an increase in the Weber number leads to an increase in the axial velocity profiles for the flow of waxy crude oil in a pipeline. A higher Weber number indicates that the surface tension forces acting on the fluid element are weaker relative to the inertial forces. This implies that surface tension forces have a reduced ability to keep the

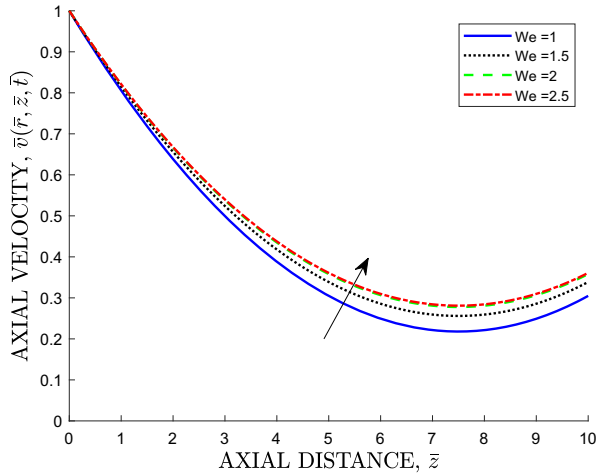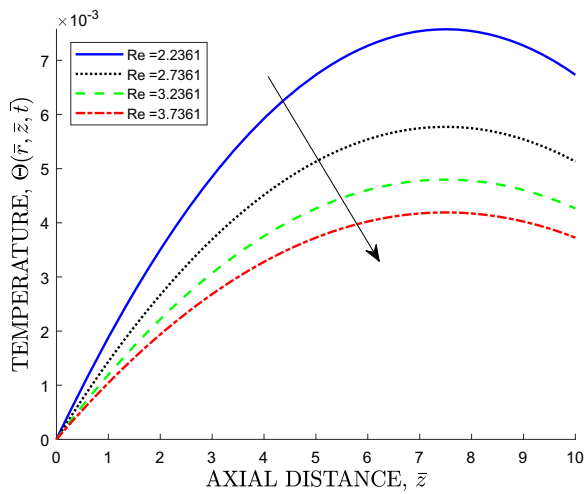**Fig. 16** Effects of varying Weber number on the axial velocity profiles

Fig. 17 Effects of varying Reynolds number on the temperature profiles

fluid element intact, making it more prone to breaking up into smaller droplets. This results in a more rapid flow of the fluid in the axial direction.

Temperature of Waxy Crude Oil

In Fig. 17, it is observed that an increase in the Reynolds number results in a decrease in the temperature profiles for the flow of waxy crude oil in a pipeline within the laminar flow regime. This phenomenon is attributed to the enhanced heat transfer due to an increase in shear stress. As the Reynolds number increases, the shear stress acting on the fluid intensifies, leading to more efficient mixing and heat transfer between the bulk of the flow and the colder pipe walls. The enhanced heat transfer due to increased shear stress leads to a flatter temperature profile, with a more uniform distribution of temperature across the pipe.

It is observed in Fig. 18 that an increase in the mass Grashof number results in an increase in the temperature profiles for the flow of waxy crude oil in a pipeline. This phenomenon is attributed to buoyancy-induced convection. As the mass Grashof number increases, the

Fig. 18 Effects of varying mass Grashof number on the temperature profiles
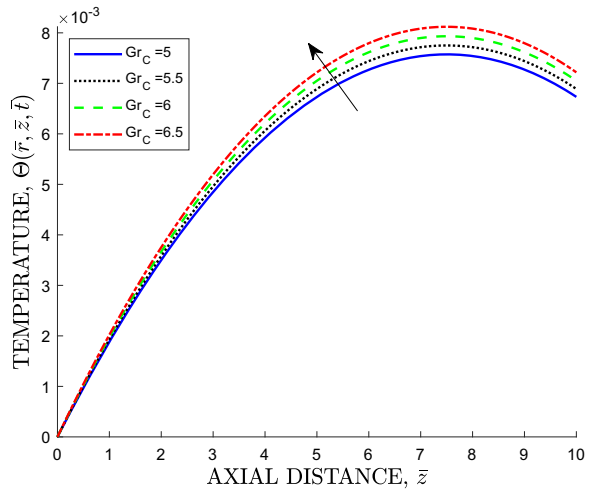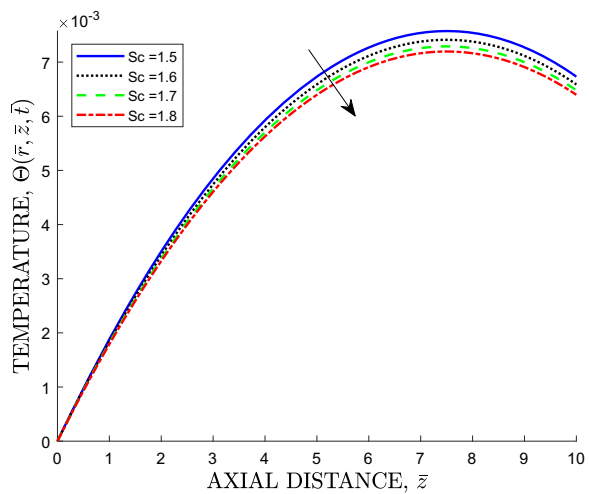

Fig. 19 Effects of varying Schmidt number on the temperature profiles

buoyancy forces acting on the denser, waxy crude oil near the pipe walls become more pronounced than the viscous forces, prompting the oil to rise towards the center of the pipe. This upward movement of the oil disrupts the flow pattern, generating swirling motions that enhance heat transfer between the fluid and the colder pipe walls. The enhanced heat transfer due to buoyancy-induced convection leads to a rise in the temperature profile near the pipe walls. This is because the swirling motions bring the colder fluid from the pipe walls into contact with the warmer fluid in the bulk of the flow, promoting heat exchange and thereby reducing the overall temperature gradient.

In Fig. 19, it is observed that an increase in the Schmidt number results in a decrease in the temperature profiles for the flow of waxy crude oil in a pipeline. This phenomenon is attributed to the suppression of buoyancy-induced convection. As the Schmidt number increases, the rate of mass transfer between the waxy crude oil and the surrounding fluid reduces. This reduced mass transfer hinders the formation of density gradients that are crucial for driving buoyancy-induced convection. Consequently, the decrease in buoyancy-induced convection

Fig. 20 Effects of varying Weber number on the temperature profiles
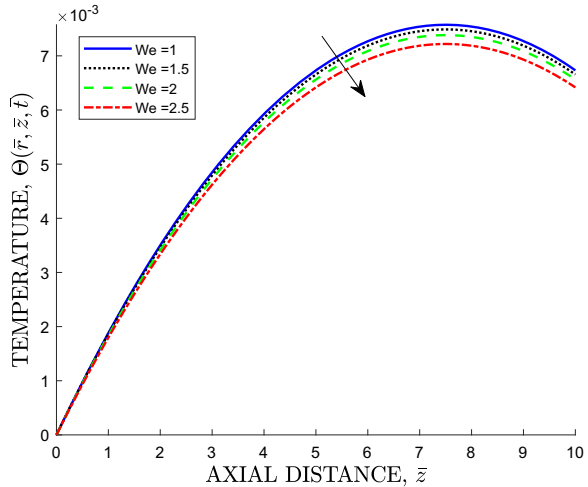
with increasing Schmidt number leads to a reduction in the overall heat transfer rate and a flattening of the temperature profile.

In Fig. 20, it is observed that an increase in the Weber number results in a decrease in the temperature profiles for the flow of waxy crude oil in a pipeline. This phenomenon is attributed to the formation of smaller oil droplets and a more dispersed flow pattern. As the Weber number increases, the inertial forces acting on the waxy crude oil become more dominant relative to surface tension forces. These enhanced inertial forces lead to the creation of smaller oil droplets and a more dispersed flow pattern. Smaller oil droplets possess a larger surface area to volume ratio, enabling them to transfer heat more efficiently to the surrounding environment. This can result in a decrease in the overall temperature of the waxy crude oil flowing in the pipeline. Additionally, a more dispersed flow pattern can reduce the amount of heat transferred from the pipeline walls to the oil. This is because the dispersed oil droplets have a lower probability of being in direct contact with the pipeline walls. This can further contribute to a decrease in the overall temperature of the waxy crude oil flowing in the pipeline.

Total Wax Concentration

It is observed in Fig. 21 that an increase in the Reynolds number results in a decrease in the total wax concentration profiles for the flow of waxy crude oil in a pipeline within the laminar flow regime. As the Reynolds number increases, the shear stresses acting on the waxy crude oil intensify, causing the elongated wax crystals to break up into smaller particles. These smaller particles have a reduced tendency to adhere to the pipe wall and are more easily entrained by the flow. As a consequence, the total wax concentration in the pipeline decreases. Additionally, increased shear stresses associated with higher Reynolds numbers enhance the mixing of the oil and wax crystals. This augmented mixing can facilitate the dissolution of more wax into the oil, further reducing the overall wax concentration. This can have advantageous implications for pipeline operations, as it can mitigate the risk of wax deposition and gelation.

In Fig. 22, it is observed that an increase in the mass Grashof number results in a decrease in the total wax concentration profiles for the flow of waxy crude oil in a pipeline. This

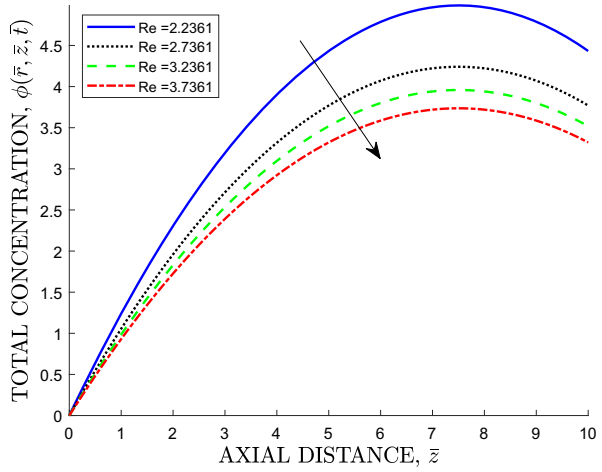**Fig. 21** Effects of varying Reynolds number on the total wax concentration profiles

Fig. 22 Effects of varying mass Grashof number on the total wax concentration profiles
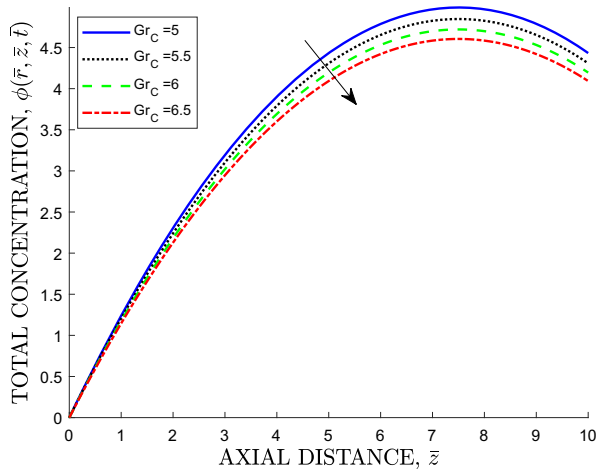

Fig. 23 Effects of varying Schmidt number on the total wax concentration profiles
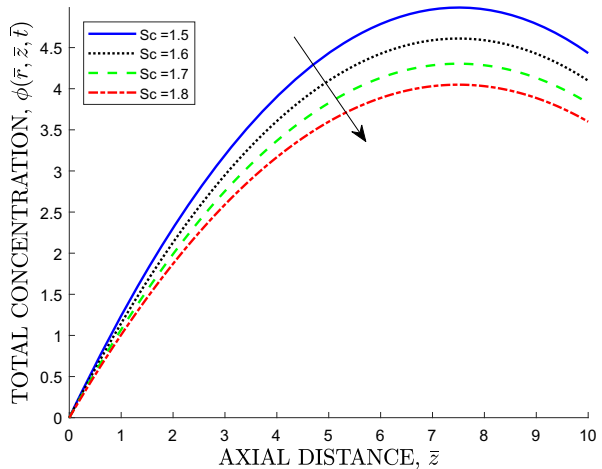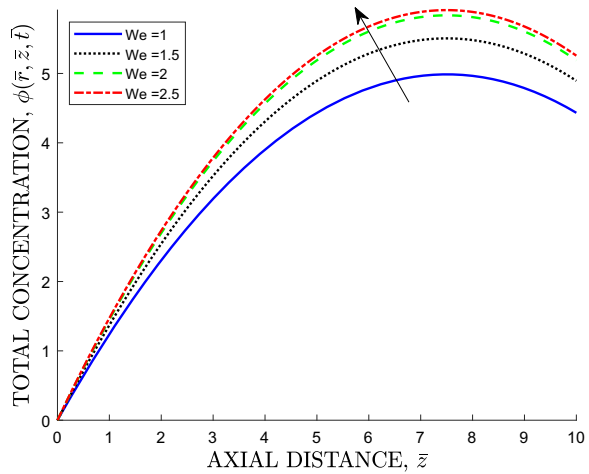
Fig. 24 Effects of varying Weber number on the total wax concentration profiles

phenomenon is attributed to the thinning of the hydrodynamic boundary layer. As the mass Grashof number increases, the buoyancy forces acting on the waxy crude oil become more pronounced than the viscous forces. This leads to a reduction in the thickness of the hydro-dynamic boundary layer near the pipe wall. A thinner hydrodynamic boundary layer reduces the likelihood of wax crystals depositing on the pipe wall. This is because the wax crystals have a shorter time window to interact with the pipe wall before being swept away by the flow. Consequently, the overall wax concentration in the pipeline decreases.

In Fig. 23, it is observed that an increase in the Schmidt number results in a decrease in the total wax concentration profiles for the flow of waxy crude oil in a pipeline. An increase in the Schmidt number indicates that the momentum diffusivity is becoming relatively more pronounced than the mass diffusivity. This implies that the flow of the oil is becoming more efficient at transporting wax crystals away from the pipe wall, facilitating enhanced mixing between the oil and wax crystals. As a consequence of this increased mixing, the wax crystals become more uniformly distributed throughout the pipeline. This results in a lower concentration of wax crystals near the pipe wall.

In Fig. 24, it is observed that an increase in the Weber number results in an increase in the total wax concentration profiles for the flow of waxy crude oil in a pipeline. This phenomenon is attributed to the increased dominance of inertial forces over surface tension forces. As the Weber number increases, flow velocities are enhanced, leading to the fragmentation of larger wax droplets into smaller ones. This increased surface area of wax droplets facilitates more efficient wax adsorption onto the pipeline walls.

Aggregation Degree of Wax

In Fig. 25, it is observed that an increase in the Reynolds number results in a decrease in the wax aggregation degree profiles for the flow of waxy crude oil in a pipeline within the lami-nar flow regime. This phenomenon is attributed to the increased dominance of inertial forces over viscous forces. As the Reynolds number increases, flow velocities are enhanced, leading to more effective mixing between the wax crystals and the surrounding oil. This improved mixing promotes a more uniform distribution of wax crystals throughout the pipeline. Con-sequently, the concentration gradient of wax crystals near the pipeline walls is reduced,

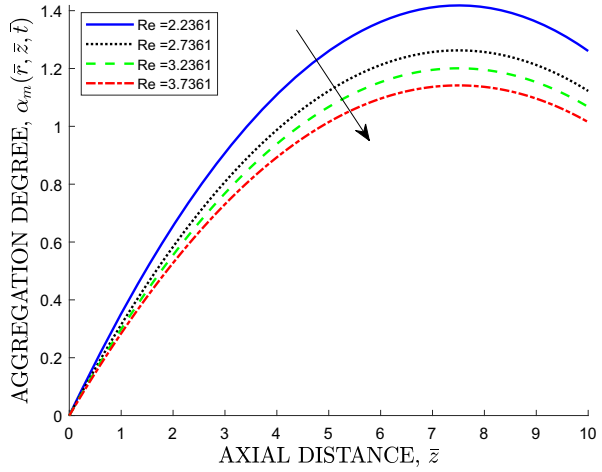**Fig. 25** Effects of varying Reynolds number on the wax aggregation degree profiles

Fig. 26 Effects of varying Schmidt number on the wax aggregation degree profiles
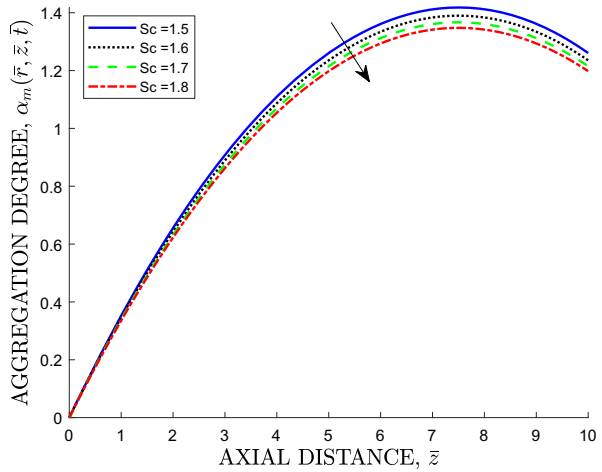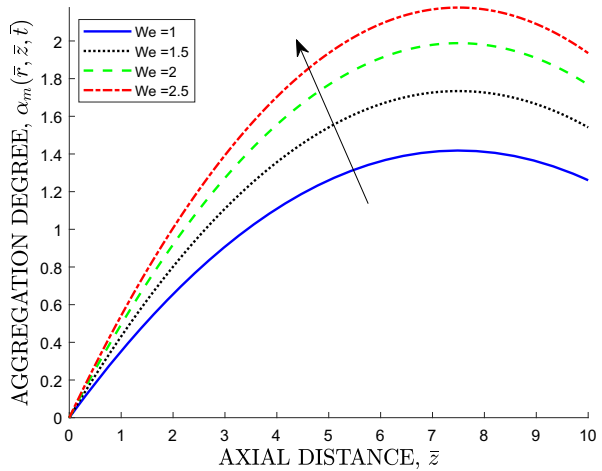

Fig. 27 Effects of varying Weber number on the wax aggregation degree profiles

hindering their accumulation and preventing the formation of large aggregates near the pipe wall.

In Fig. 26, it is observed that an increase in the Schmidt number results in a decrease in the wax aggregation degree profiles for the flow of waxy crude oil in a pipeline. This phenomenon is attributed to the enhanced dominance of momentum diffusivity over mass diffusivity. As the Schmidt number increases, the oil becomes more efficient at transporting wax crystals away from the pipe wall, hindering their accumulation and preventing the formation of large aggregates. This can help to mitigate wax deposition and gelation in crude oil pipelines.

In Fig. 27, it is observed that an increase in the Weber number results in an increase in the wax aggregate degree profiles for the flow of waxy crude oil in a pipeline. This phenomenon is attributed to the enhanced dominance of inertial forces over surface tension forces. The increased inertial forces cause the wax crystals to break up, leading to the formation of smaller wax droplets. Smaller wax droplets possess a larger surface area to volume ratio compared to their larger counterparts. This increased surface area facilitates the adhesion of wax crystals to each other, promoting the formation of aggregates. Additionally, the smaller wax droplets are more easily entrained by the flow, bringing them into closer contact and further enhancing aggregation.

Skin Friction Coefficient and Rates of Heat and Mass Transfer

The local skin friction coefficient (C_fRe), the local Nusselt number (Nu_z), and the local Sherwood number (Sh_z) are computed. The skin friction coefficient represents the drag force exerted by the fluid on the pipeline wall. The Nusselt number quantifies the rate of heat transfer between the fluid and the pipeline wall. The Sherwood number measures the rate of mass transfer between the fluid and the pipeline wall.

The flow parameters which are investigated are Reynolds number (Re), thermal Grashof number (Gr_T), mass Grashof number (Gr_C), Eckert number (Ec), Schmidt number (Sc), and Weber number (We). These parameters are varied on the local coefficient of skin friction, local Nusselt number and local Sherwood number and their numerical values are presented in Table 1.

From the table, the following observations are noted:

 i) An increase in the Reynolds number causes an increase in the skin friction coefficient but leads to a decrease in the Nusselt number and Sherwood number. The skin friction coefficient increases due to increased turbulence, which enhances the interaction between the fluid and the wall. However, the enhancement of turbulence also leads to the formation of a thicker boundary layer, which acts like an insulating barrier and reduces the heat and mass transfer rates, resulting in a decrease in the Nusselt number and Sherwood number.
 ii) An increase in the thermal Grashof number increases the skin friction coefficient and Sherwood number, but has a minimal effect on the Nusselt number. The skin friction coefficient and Sherwood number increase due to enhanced turbulence and mixing. However, the formation of a wax layer on the pipe wall can degrade the increase in heat transfer caused by turbulence.
 iii) An increase in the mass Grashof number has a positive effect on the skin friction coefficient, Nusselt number, and Sherwood number. This positive effect is attributed to enhanced turbulence and mixing, which are caused by the stronger buoyancy force arising from the density difference between the oil and the wax crystals. The enhanced turbulence facilitates friction between fluid layers, promotes mixing of hot and cold fluid layers, and facilitates mass transfer between the bulk flow and the pipe wall.

Table 1 Skin friction coefficient and rates of heat and mass transfer for various values of the parameters Re, Gr_T, Gr_C, Ec, Sc, and We

Re	Gr_T	Gr_C	Ec	Sc	We	C_fRe	Nu_z	Sh_z
2.24	5	5	1.2	1.5	1.0	0.1230	1.9907	1.3916
3.24	5	5	1.2	1.5	1.0	0.1874	1.9912	1.3206
4.24	5	5	1.2	1.5	1.0	0.2926	1.9911	1.2494
5.24	5	5	1.2	1.5	1.0	0.4022	1.9908	1.1864
2.24	10	5	1.2	1.5	1.0	0.1246	1.9907	1.3926
2.24	15	5	1.2	1.5	1.0	0.1262	1.9907	1.3935
2.24	20	5	1.2	1.5	1.0	0.1277	1.9907	1.3944
2.24	5	10	1.2	1.5	1.0	0.2038	1.9915	1.4182
2.24	5	15	1.2	1.5	1.0	0.2793	1.9921	1.4438
2.24	5	20	1.2	1.5	1.0	0.3495	1.9925	1.4683
2.24	5	5	2.7	1.5	1.0	0.1233	1.9890	1.3922
2.24	5	5	4.2	1.5	1.0	0.1236	1.9874	1.3928
2.24	5	5	5.7	1.5	1.0	0.1238	1.9857	1.3933
2.24	5	5	1.2	3.0	1.0	0.1098	1.9906	1.4851
2.24	5	5	1.2	4.5	1.0	0.1055	1.9905	1.5162
2.24	5	5	1.2	6.0	1.0	0.1033	1.9905	1.5318
2.24	5	5	1.2	1.5	1.5	0.1113	1.9919	1.5007
2.24	5	5	1.2	1.5	2.0	0.1047	1.9925	1.5614
2.24	5	5	1.2	1.5	2.5	0.1004	1.9929	1.6002

iv) An increase in the Eckert number causes an increase in the skin friction coefficient and Sherwood number but decreases the Nusselt number. This is because the increased kinetic energy to enthalpy ratio leads to a higher fluid velocity, which enhances turbulence and mass transfer. However, the formation of a wax layer on the pipe wall acts like an insulator, reducing heat transfer between the oil and the pipe wall, therefore decreasing the Nusselt number.

v) An increase in the Schmidt number causes a decrease in the skin friction coefficient and Nusselt number but increases the Sherwood number. This is because the increased momentum transfer rate relative to mass diffusivity reduces the shear stress between the fluid and the pipe wall, reduces the thickness of the thermal boundary layer (which in turn reduces the rate of heat transfer and decreases the Nusselt number), and increases the rate of mass transfer between the bulk flow and the pipe wall, so increasing the Sherwood number.

vi) An increase in the Weber number decreases the skin friction coefficient but it increases the Nusselt number and Sherwood number. This is because an increase in the Weber number decreases the contact area between the fluid and the pipe wall (which leads to a decrease in the shear stress between the fluid and the pipe wall, hence reducing the skin friction coefficient), enhances turbulence (which promotes the heat transfer between the oil and the pipe wall, hence leading to an increase in the Nusselt number), and enhances the mass transfer rate between the bulk flow and the pipe wall, hence increasing the Sherwood number.

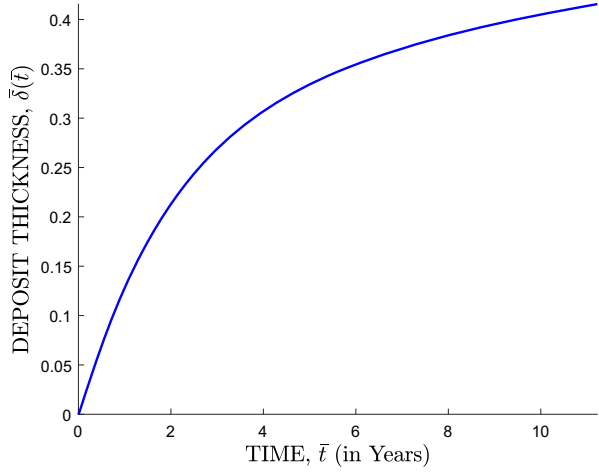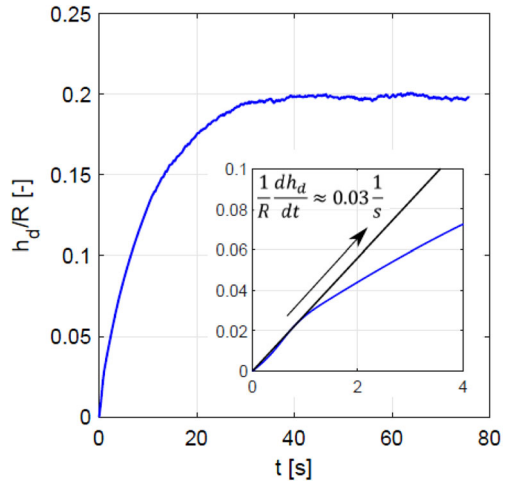**Fig. 28** Deposit thickness profile (Present study)

Fig. 29 Average wax deposit thickness profile (Magnini and Matar [19])

Validation

The model's predictive capabilities in this research are validated against experimental data from Magnini and Matar [19]. In particular, the wax deposit thickness is compared in both studies, as shown in Figs. 28 and 29. It is observed that the deposit thickness profiles follow a similar trend as time increases. This validation demonstrates the model's ability to accurately predict wax deposition under various flow conditions.

Summary and Conclusions

This study presents a novel computational model for predicting wax deposition in crude oil pipelines, accounting for the complex interplay of multiphase flow scenarios involving water-in-oil emulsions, wax precipitation kinetics, molecular diffusion, and shear dispersion. The model equations, in the form of coupled nonlinear partial differential equations governing

the flow, are discretized in time using a second-order semi-implicit scheme and in space using the bivariate spectral collocation method. The model's predictive capabilities have been thoroughly evaluated by investigating the impact of various flow parameters, including the Reynolds number (Re), Grashof number (Gr), Schmidt number (Sc), and Weber number (We), on the flow variables, wall shear stress, and heat and mass fluxes. The following conclusions can be drawn from the results of this research:

- Wax deposit thickness and weight fraction of wax crystals in the gel layer reach steady-state values of 0.4 and 0.012, respectively. These steady-state values indicate that a balance has been reached between the deposition and removal processes of wax crystals.
- Wax deposit thickness increases by at most 5.0% with increasing Reynolds number from 2.0 to 6.5, but decreases by at most 10.0% with increasing mass Grashof number from 4 to 16. Similarly, higher Schmidt numbers (Sc > 1) and Weber numbers (We > 1) tend to mitigate wax deposition by at most 15.0% and 6.0%, respectively.
- The axial velocity of waxy crude oil decreases by at most 25% with increasing Reynolds number from 2.2361 to 3.7361, increases by at most 10% with increasing mass Grashof number from 5 to 6.5, decreases by at most 10% with increasing Schmidt number from 1.5 to 1.8, and increases by at most 8% with increasing Weber number from 1.0 to 2.5.
- Skin friction coefficient increases from 0.1230 to 0.4022 with increasing Reynolds number from 2.24 to 5.24, but increases from 0.1230 to 0.1277 with increasing mass Grashof number from 5 to 20, and decreases from 0.1230 to 0.1004 with increasing Weber number from 1.0 to 2.5.
- The Nusselt number decreases from 1.9907 to 1.1864 with increasing Reynolds number from 2.24 to 5.24, but increases from 1.9907 to 1.9925 with increasing mass Grashof number from 5 to 20, and decreases from 1.9907 to 1.9929 with increasing Weber number from 1.0 to 2.5.
- The Sherwood number increases from 1.3916 to 1.3944 with increasing mass Grashof number from 5 to 20, but increases from 1.3916 to 1.6002 with increasing Weber number from 1.0 to 2.5.

These insights offer valuable guidance for optimizing pipeline operations, designing effective wax control strategies, and enhancing pipeline integrity management in field-scale crude oil transportation systems. Specifically, pipeline operators can use the model to identify critical flow parameters that influence wax deposition and optimize these parameters to minimize wax accumulation. Additionally, the model can be used to evaluate the effectiveness of various wax control strategies, such as the use of chemical additives and pipeline pigging, and select the most appropriate strategy for a given pipeline configuration and crude oil composition. The inclusion of wax deposition modeling in pipeline design and operation will help to ensure the reliable and efficient transportation of crude oil.

Data Availability Data sharing is not applicable to this article as no datasets were generated or analyzed during the current study.

Code Availability The findings of this study are supported by MATLAB® source code which can be availed by the corresponding author upon reasonable request.

Declarations

Conflict of interest The authors declare that they have no competing interests.

Ethical approval Not applicable.

Consent to participate Not applicable.

Consent for publication Not applicable.

References

1. Alnaimat, F., Ziauddin, M.: Wax deposition and prediction in petroleum pipelines. J. Petrol. Sci. Eng. **184**, 106385 (2020)
2. Jalalnezhad, M.J., Kamali, V.: Development of an intelligent model for wax deposition in oil pipeline. J. Pet. Explor. Prod. Technol. **6**, 129–133 (2016)
3. Azevedo, L., Teixeira, A.: A critical review of the modeling of wax deposition mechanisms. Pet. Sci. Technol. **21**(3–4), 393–408 (2003)
4. Sousa, A., Matos, H., Guerreiro, L.: Preventing and removing wax deposition inside vertical wells: a review. J. Pet. Explor. Prod. Technol. **9**, 2091–2107 (2019)
5. Chang, S.E., Stone, J., Demes, K., Piscitelli, M.: Consequences of oil spills: a review and framework for informing planning. Ecol. Soc. **19**, 2 (2014)
6. Bonvicini, S., Antonioni, G., Morra, P., Cozzani, V.: Quantitative assessment of environmental risk due to accidental spills from onshore pipelines. Process Saf. Environ. Prot. **93**, 31–49 (2015)
7. Michel, J., Fingas, M.: Oil spills: Causes, consequences, prevention, and countermeasures, in Fossil fuels: current status and future directions, pp. 159–201. World Scientific, Singapore (2016)
8. Valinejad, R., Nazar, A.R.S.: An experimental design approach for investigating the effects of operating factors on the wax deposition in pipelines. Fuel **106**, 843–850 (2013)
9. Quan, Q., Wang, W., Wang, P., Yang, J., Gao, G., Yang, L., Gong, J.: Effect of oil temperature on the wax deposition of crude oil with composition analysis. Braz. J. Chem. Eng. **33**, 1055–1061 (2016)
10. Kim, D.Y., Kim, W.B., Choi, J., Sim, H.S., Moon, J.H.: Modeling consolidation of wax deposition for progressive cavity pump using computational fluid dynamics. Eng. Sci. Technol. Int. J. **41**, 101384 (2023)
11. K. Mrinal, M. H. Siddique, and A. Samad, A transient 3d cfd model of a progressive cavity pump. in Turbo Expo: Power for Land, Sea, and Air, vol. 49873. American Society of Mechanical Engineers, New York City, 2016, p. V009T24A009
12. Waheed, S.E., Megahed, A.M.: Melting heat transfer effects on flow of a micropolar fluid with heat generation (absorption) in slip flow regime. Appl. Math. Inf. Sci. **16**(1), 35–44 (2022)
13. Singh, P., Venkatesan, R., Fogler, H.S., Nagarajan, N.: Formation and aging of incipient thin film wax-oil gels. AIChE J. **46**(5), 1059–1074 (2000)
14. Stubsjøen, M.: Analytical and numerical modeling of paraffin wax in pipelines. Master's thesis, Institutt for petroleumsteknologi og anvendt geofysikk, 2013
15. Fusi, L.: On the stationary flow of a waxy crude oil with deposition mechanisms. Nonlinear Anal. Theory Methods Appl. **53**(3–4), 507–526 (2003)
16. Banki, R., Hoteit, H., Firoozabadi, A.: Mathematical formulation and numerical modeling of wax deposition in pipelines from enthalpy-porosity approach and irreversible thermodynamics. Int. J. Heat Mass Transf. **51**(13–14), 3387–3398 (2008)
17. Zhang, L., Qu, S., Wang, C., Guan, B.: Prediction temperature field and wax deposition based on heat-fluid coupling method. J. Pet. Explor. Prod. Technol. **9**, 1–6 (2018)
18. Ying, X., Xin, N., Qinglin, C., Zhonghua, D., Xiaoyan, L., Yang, L., Cong, L.: Phase-change heat transfer analysis of shutdown overhead pipeline. Case Stud. Thermal Eng. **13**, 100399 (2019)
19. Magnini, M., Matar, O.K.: Fundamental study of wax deposition in crude oil flows in a pipeline via interface-resolved numerical simulations. Ind. Eng. Chem. Res. **58**(47), 21797–21816 (2019)
20. Boucetta, R., Haddad, Z., Zamoum, M., Kessal, M., Arıcı, M.: Numerical investigation of wax deposition features in a pipeline under laminar flow conditions. J. Petrol. Sci. Eng. **217**, 110929 (2022)
21. Yang, H., Vanka, S.P., Thomas, B.G.: Mathematical modeling of multiphase flow in steel continuous casting. ISIJ Int. **59**(6), 956–972 (2019)

22. Zheng, S., Saidoun, M., Palermo, T., Mateen, K., Fogler, H.S.: Wax deposition modeling with considerations of non-newtonian characteristics: application on field-scale pipeline. Energy Fuels **31**(5), 5011–5023 (2017)
23. Ochieng, F.O., Kinyanjui, M.N., Abonyo, J.O., Kiogora, P.R.: Mathematical modeling of wax deposition in field-scale crude oil pipeline systems. J. Appl. Math. **2022**, 1–13 (2022)
24. Koledintseva, M., DuBroff, R., Schwartz, R.: A maxwell garnett model for dielectric mixtures containing conducting particles at optical frequencies. Prog. Electromagn. Res. **63**, 223–242 (2006)
25. Cragoe, C.S.: Thermal Properties of Petroleum Products: November 9, 1929.Washington: US Government Printing Office, 1929, 97
26. Al-Ahmad, M., Al-Fariss, T., Obaid-ur Rehman, S.: Solubility studies on a paraffin wax in base oils. Fuel **69**(3), 293–296 (1990)
27. Motsa, S., Makukula, Z., Shateyi, S.: Numerical investigation of the effect of unsteadiness on three-dimensional flow of an oldroyb-b fluid. PLoS ONE **10**(7), e0133507 (2015)
28. Trefethen, L.N.: Spectral methods in MATLAB.Philadelphia: SIAM, 2000